Gas confinement in compartmentalized coordination polymers for highly selective sorption

Mónica Giménez-Marqués,[1] Néstor Calvo Galve,[1] Miguel Palomino,[2] Susana Valencia,[2] Fernando Rey,[2] Germán Sastre,[2] Iñigo J. Vitórica-Yrezábal,[3] Mónica Jiménez-Ruiz,[4] J. Alberto Rodríguez-Velamazán,[4,5] Miguel A. González,[4] José L. Jordá,[2] Eugenio Coronado,[1] Guillermo Mínguez Espallargas[1]*.

[1] Instituto de Ciencia Molecular (ICMol), Universidad de Valencia, c/ Catedrático José Beltrán, 2, 46980 Paterna, Spain.

[2] Instituto de Tecnología Química (UPV-CSIC), Universidad Politécnica de Valencia – Consejo Superior de Investigaciones Científicas, Av. de los Naranjos s/n, 46022 Valencia, Spain

[3] School of Chemistry, University of Manchester, Oxford Road, Manchester, M13 9PL, UK

[4] Institut Laue-Langevin, 38042 Grenoble Cedex 9, France

[5] Instituto de Ciencia de Materiales de Aragón (ICMA), CSIC – Universidad de Zaragoza, 50009 Zaragoza, Spain

Supporting Information

Contents

S1. Synthesis

All reagents were commercially available and used without further purification. Solvents were dried and purified before use, according to standard procedures. The ligand btzx, (1,4-bis(tetrazol-1-ylmethyl)benzene), was prepared as previously reported.[1] All synthesis were carried out using standard airless techniques. ^{1}H NMR spectra was recorded on a Bruker DPX300 (300 MHz) spectrometer. Proton (^{1}H) chemical shifts are reported in parts per million (δ) and referenced internally with respect to the protic solvent impurity. Elemental analysis was carried out at the Centro de Microanálisis Elemental, Universidad Complutense de Madrid. Infrared spectra were recorded in a FT-IR Nicolet 5700 spectrometer in the 4000–400 cm^{-1} range using powdered samples diluted in KBr pellets. Thermogravimetric analysis were carried out with a Mettler Toledo TGA/SDTA 851 apparatus in the 25–800 °C temperature range under a 10 °C·min^{-1} scan rate and an air flow of 30 ml·min^{-1}. Microwave synthesis were carried out with a CEM Focused Microwave Synthesis System operating at 200 MHz and 82 ºC.

Caution! Perchlorate salts are explosive (especially if they are dry) and should be handled with extreme caution.

S1.1. Synthesis of 1,4-bis(tetrazol-1-ylmethyl)benzene (btzx). *p*-Xylylenediamine (5 g, 0.037 mol), triethylortoformate (54 g, 0.363 mol) and sodium azide (4.79 g, 0.074 mol) were dissolved in acetic acid (90 mL) and heated at 90 ºC for 2 days. After cooling down to room temperature, the solvent was evaporated at reduced pressure. The remaining yellow solid was washed with methanol and water yielding the ligand as a white powder. Yield = 68 %; ^{1}H NMR (300 MHz, [D6]DMSO): d=5.7 (s, 4H; ttz-CH$_2$-ph), 7.4 (s, 4H; ph), 9.5 ppm (s, 2H; ttz); IR: = 3118 cm^{-1} (n Cttz-H).

S1.2. Synthesis of [Fe(btzx)$_3$](ClO$_4$)$_2$ (CCP-1). A solution of Fe(ClO$_4$)$_2$·xH$_2$O (112 mg) in 5 mL of MeCN was added into a suspension of btzx (152 mg, 0.63 mmol) in 40 mL of MeCN containing ascorbic acid (*ca*. 10 mg). The resulting milky suspension was refluxed and stirred for 4 h. A white crystalline precipitate appeared during the reaction. After cooling down to room temperature, the white powder was filtered and washed with MeCN. Alternative synthesis by microwaves was carried out in a CEM Focused Microwave Synthesis System. Fe(ClO$_4$)$_2$·xH$_2$O (16.4 mg), btzx (22.8 mg, 0.09 mmol) and 6 mL of MeCN were introduced in a microwave vial and the reaction was carried out with 200 MHz and 82 ºC during 5 minutes. The reaction was cooled down and a white precipitate appeared after few hours. Phase purity was established by X-ray powder diffraction (*vide infra*). Yield = 71 %. Anal. calc. $C_{30}H_{30}FeN_{24}Cl_2O_8$ (981.47): C, 36.71; H, 3.08; N, 34.25 %. Found: C, 36.98; H, 3.16; N, 34.03 %.

S1.3. Synthesis of [Fe(btzx)$_3$](BF$_4$)$_2$ (CCP-2). CCP-2 was synthesized in a procedure analogous to that of **CCP-1** except that Fe(BF$_4$)$_2$·6H$_2$O (152 mg, 0.45 mmol) was used instead. A white crystalline precipitate was collected and washed with MeCN. Alternative synthesis by microwaves was carried out in a CEM Focused Microwave Synthesis System. Fe(BF$_4$)$_2$·6H$_2$O (21.7 mg, 0.06 mmol), btzx (22.8 mg, 0.09 mmol) and 6 mL of MeCN were introduced in a microwave vial and the reaction was carried out with 200 MHz and 82 ºC during 5 minutes. The reaction was cooled down and a white precipitate appeared after few hours. Phase purity was established by X-ray powder diffraction (*vide infra*). Yield = 62 %. Anal. calc. $C_{30}H_{30}FeN_{24}B_2F_8$ (956.18): C, 37.68; H, 3.16; N, 35.16 %. Found: C, 38.81; H, 3.37; N, 35.34 %.

S2. Single-Crystal X-Ray Diffraction.

The crystal structure of compound **CCP-1** has been previously reported by us both in the high spin and low spin states.[S1] A single crystal of **CCP-2** was mounted on glass fibre using a viscous hydrocarbon oil to coat the crystal and then transferred directly to the cold nitrogen stream for data collection. X-ray data was collected on the same crystal at 240 K (**CCP-2–HS**) and then at 120 K (**CCP-2–LS**) on a Supernova diffractometer equipped with a graphite-monochromated Enhance (Mo) X-ray Source (λ = 0.71073 Å). The program CrysAlisPro, Oxford Diffraction Ltd., was used for unit cell determinations and data reduction. Empirical absorption correction was performed using spherical harmonics, implemented in the SCALE3 ABSPACK scaling algorithm. Crystal structures were solved and refined against all F^2 values using the SHELXTL suite of programs.[S2] All non-hydrogen atoms were refined anisotropically. Hydrogen atoms were placed in calculated positions, refined using idealized geometries (riding model) and assigned fixed isotropic displacement parameters. The disordered anions were modelled over two orientations with fixed thermal parameters, with occupancies 63.9(22):36.1(22) and 62.8(17):37.2(17) for **CCP-2–HS** and **CCP-2–LS**, respectively. CCDC-1439096 (**CCP-2–HS**) and -1439097 (**CCP-2–LS**) contain the supplementary crystallographic data for this paper. A summary of selected bond distances and angles is provided in Table S1, and a summary of the data collection and structure refinements is provided in Table S2.

Table S1. Selected bond lengths (Å), angles (º), metal-metal distances, octahedral distortion parameters and voids for **CCP-1** and **CCP-2** in the HS (240 K) and LS (120 K) states.

	CCP-1–LS	**CCP-1–HS**	**CCP-2–LS**	**CCP-2–HS**
Fe–N	1.996(4)	2.160(6)	1.933(4)	2.150(8)
N–Fe–N	90.18(16)	90.4(2)	90.7(2)	90.6(3)
	89.82(16)	89.6(2)	89.3(2)	89.4(3)
	180.00	180.0	180.0(3)	180.0(3)
Fe···Fe $_{\text{intra}}$	11.5752(9)	11.7881(12)	11.4814(8)	11.6540(15)
Fe···Fe $_{\text{inter}}$	10.3668(4)	10.5117(7)	10.3690(5)	10.4852(10)
Σ [a]	2.4	4.8	4.8	9.6
Discrete void (Å^3) [b]	117	132	121	140
Voids % [c]	10.8	11.7	11.3	12.4

[a] Octahedral distortion parameter $\Sigma = \Sigma_1^{12}(|90-\varphi i|)$ [Σ = 0° for an ideal octahedron; φi represents the twelve smallest L–M–L angles]

[b] Solvent accessible area (Å^3)

[c] Total potential solvent area volume per unit cell volume

Table S2. Crystallographic data for **CCP-2–HS** and **CCP-2–LS**.

Compound	**CCP-2–HS**	**CCP-2–LS**
Empirical formula	$C_{30}H_{30}N_{24}B_2F_8Fe$	$C_{30}H_{30}N_{24}B_2F_8Fe$
Formula weight	956.25	956.25
Crystal color	Colorless	Pink
Crystal size (mm^3)	0.05 × 0.05 × 0.02	0.05 × 0.05 × 0.02
Temperature (K)	240(2)	120(2)
Crystal system, Z	Hexagonal, 2	Hexagonal, 2
Space group	$P6_3/m$	$P6_3/m$
a (Å)	10.4852(10)	10.3690(5)
b (Å)	10.4852(10)	10.3690(5)
c (Å)	23.308(3)	22.9628(15)
α (°)	90.00	90.00
β (°)	90.00	90.00
γ (°)	120.00	120.00
V (Å^3)	2219.2(5)	2138.1(2)
ρ_{calc} (Mg/m^3)	1.431	1.485
μ(Mo$_{K\alpha}$) (mm^{-1})	0.428	0.444
θ range (°)	2.83 – 25.11	3.50 – 25.01
Reflns collected	4614	9643
Independent reflns (R_{int})	1400 (0.1645)	1300 (0.1235)
Reflns used in refinement, n	1400	1300
L. S. parameters, p/ restraints, r	113/112	109/22
$R1(F)$,[a] $I>2\sigma(I)$	0.1085	0.1090
$wR2(F^2)$,[b] all data	0.3038	0.2978
$S(F^2)$,[c] all data	1.055	1.080

[a] $R1(F) = \Sigma(|F_O| - |F_C|)/\Sigma|F_O|$; [b] $wR2(F^2) = [\Sigma w(F_O^2 - F_C^2)^2/\Sigma wF_O^4]^{½}$; [c] $S(F^2) = [\Sigma w(F_O^2 - F_C^2)^2/(n + r - p)]^{½}$

S3. Powder X-Ray Diffraction – phase purity.

Phase purity of **CCP-1** and **CCP-2** was established by PXRD. Polycrystalline samples of **CCP-1** and **CCP-2** were lightly ground in an agate mortar and pestle and filled into a 0.5 mm borosilicate capillary. Data were collected at room temperature in the 2θ range 2–60 ° on an Empyrean PANalytical powder diffractometer, using Cu K_α radiation. Pawley refinements[S3] were performed using the TOPAS computer program[S4] and revealed an excellent fit to a one-phase model, indicating the absence of any other detectable crystalline phases. The observed and calculated diffraction patterns for the refined crystal structures are shown in Figure S1. Pawley refinements converged to R_{wp} = 0.0264, R_{wp}' = 0.0961 and gof = 1.461 for **CCP-1** and R_{wp} = 0.0227, R_{wp}' = 0.0934 and gof = 1.206 for **CCP-2** (R_{wp}' is the background subtracted R_{wp}).

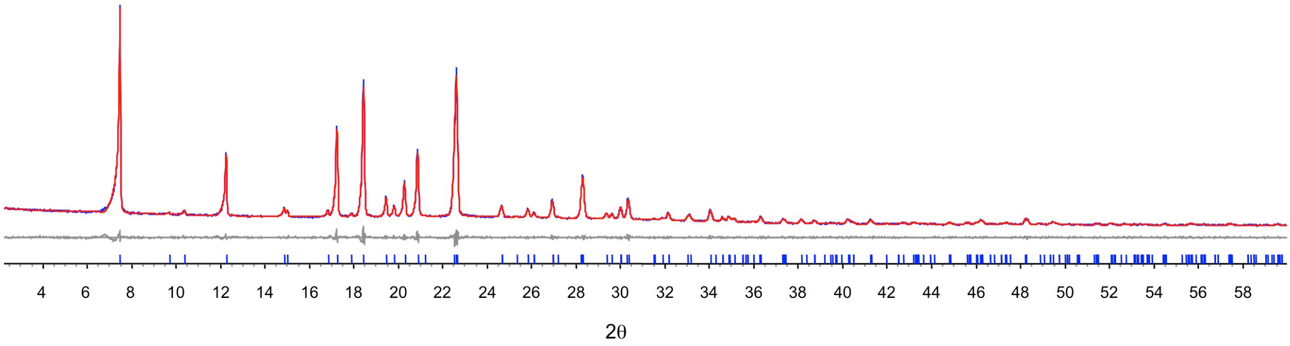

(a)

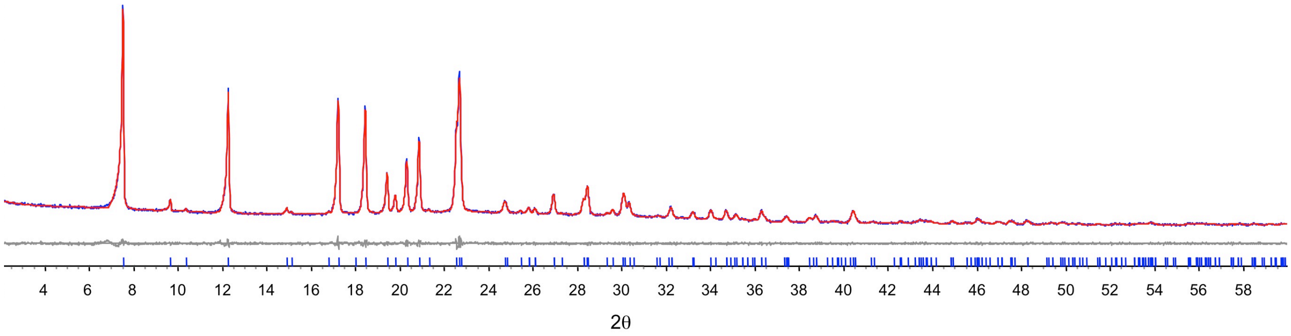

(b)

Figure S1. Observed (blue) and calculated (red) profiles and difference plot [($I_{obs} - I_{calcd}$)] (grey) of the Pawley refinements for **CCP-1** (a) and **CCP-2** (b) (2θ range 2.0–60.0 °; maximum resolution 1.54 Å).

S4. Powder X-ray diffraction under variable temperature (VT-PXRD).

In order to cover the hysteresis loop, X-ray diffractograms were recorded every 5 K when cooling from 210 to 190 K and then when warming up from 190 to 210 K with additional recordings at HS (300K) and LS (150k). Polycrystalline samples of **CCP-1** and **CCP-2** were lightly ground in an agate mortar and pestle and filled into a 0.5 mm borosilicate capillary. Data were collected at room temperature in the 2θ range 5–60 ° on an Empyrean PANalytical powder diffractometer, using Cu K_α radiation. Low-temperature measurements were achieved with an Oxford Cryosystems N_2 cryostream, which provided isothermal experiments at different temperatures. Pawley refinements[S3] were performed using the TOPAS computer program[S4] and unit cell temperature dependence was determined (see Tables S3 and S4 and Figure S2).

Temperature-dependent X-ray powder diffraction data from temperature-dependent studies can be extremely useful in the characterization of the type of spin transition (continuous or discontinuous) and for determining changes of the lattice parameters. In order to examine these parameters, X-ray variable temperature experiments have been performed on crystalline powdered samples of **CCP-1** and **CCP-2**. Powder patterns were collected at 300, 210, 205, 200, 195, 190 and 150 K both in the cooling and the heating mode. Pawley refinements were carried out on each individual scan, in which profile parameters, background and unit-cell parameters were refined. The unit-cell temperature dependence shows that the spin transition corresponds to a reversible modification of the unit cell volume of 5.1 and 4.6 % for **CCP-1** and **CCP-2** respectively. This difference in volume variation can be discussed in terms of anisotropy of the unit cell modification at the spin transition (Figure S2). Several considerations can be highlighted: i) for each compound the *c* parameter presents a larger variation (−2.0 and −2.1 % for **CCP-1** and **CCP-2** respectively) than the *a* and *b* parameters (−1.6 % and −1.3 % for **CCP-1** and **CCP-2** respectively); ii) the *c* parameter decreases similarly in both systems from HS to LS; iii) *a* and *b* parameters in each system are affected slightly different by the transition. These facts can be explained by careful analysis of the crystal structures. For **CCP-1** and **CCP-2** the higher variation along the *c* parameter compared with the *a* and *b* parameters is essentially a consequence of the linear arrangement of the chains, which run parallel to the crystallographic *c*-axis. As expected, the major change of the unit cell upon spin transition occurs along the chains where all the Fe–N bonds are propagated. For Fe^{II} complexes the t_{2g} orbitals are of non-bonding character, whereas the e_g orbitals are anti-bonding. Therefore, the metal-ligand bond length is significantly higher in the HS state than in the LS state, because in the former the antibonding orbitals are populated. In addition, the variation of the *c* parameter is equivalent in the two compounds, which is unsurprising given the similarity of the chains. However, both *a* and *b* parameters vary in a different manner for each system. This can be explained since the *a* and *b* parameters form the plane in which the anions are located and each anion interacts differently with the framework. These results support the absence of a structural phase transition accompanying the spin crossover phenomenon as previously determined by single crystal X-ray diffraction studies. Additionally, variable temperature powder X-ray experiments further confirm the different spin states of the Fe^{II} centres by means of unit cell variation.

Table S3. Unit cell parameters and refinement information from Pawley fitness from VT-PXRD on **CCP-1**.

T (K)	a, b (Å)	c (Å)	R_{wp}	R_{wp}'	gof
300	10.50905(19)	23.5994(12)	0.0258	0.0782	1.581
210	10.4478(2)	23.4625(11)	0.0258	0.0758	1.606
205	10.4300(2)	23.3928(12)	0.0255	0.0762	1.585
200	10.4030(2)	23.2844(15)	0.0254	0.0751	1.577
195	10.3837(2)	23.2070(12)	0.0262	0.0766	1.628
190	10.37365(19)	23.1744(11)	0.0271	0.0772	1.668
150	10.34440(17)	23.1209(10)	0.0284	0.0814	1.767
190	10.37308(19)	23.1728(11)	0.0274	0.0777	1.673
195	10.3831(2)	23.2062(12)	0.0262	0.0762	1.610
200	10.4028(2)	23.2832(14)	0.0255	0.0756	1.576
205	10.4297(2)	23.3926(12)	0.0260	0.0767	1.607
210	10.4469(2)	23.4599(12)	0.0255	0.0762	1.592
300	10.5087(2)	23.5993(12)	0.0259	0.0790	1.610

Table S4. Unit cell parameters and refinement information from Pawley fitness from VT-PXRD on **CCP-2**.

T (K)	a, b (Å)	c (Å)	R_{wp}	R_{wp}'	gof
300	10.5139(2)	23.3911(15)	0.0205	0.0722	1.275
210	10.4616(2)	23.2217(13)	0.0203	0.0704	1.265
205	10.4505(2)	23.1779(13)	0.0205	0.0720	1.282
200	10.4351(2)	23.1141(12)	0.0204	0.0719	1.284
195	10.4208(2)	23.0546(12)	0.0203	0.0724	1.290
190	10.40827(19)	23.0036(11)	0.0205	0.0707	1.298
150	10.37691(18)	22.9063(10)	0.0212	0.0727	1.353
190	10.40821(18)	23.0036(11)	0.0209	0.0718	1.312
195	10.41985(19)	23.0492(11)	0.0210	0.0724	1.303
200	10.4346(2)	23.1123(12)	0.0207	0.0716	1.276
205	10.4494(3)	23.1746(17)	0.0234	0.0819	1.433
210	10.4603(2)	23.2174(14)	0.0217	0.0746	1.295
300	10.5136(2)	23.3908(14)	0.0209	0.0720	1.244

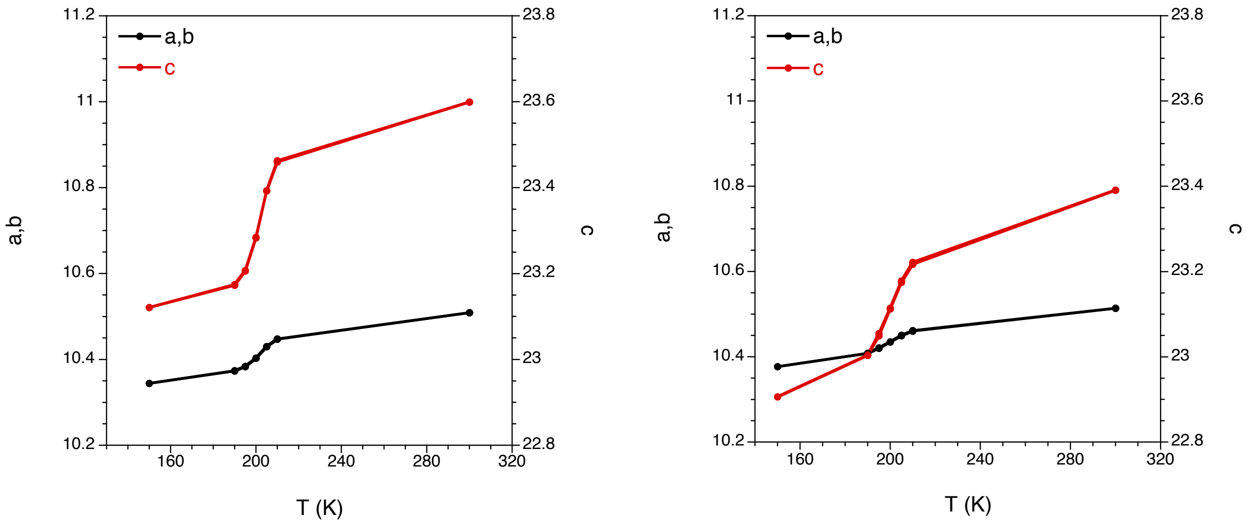

(a) (b)

Figure S2. Variation of unit cell parameters for **CCP-1** (a) and **CCP-2** (b).

S5. Powder X-ray diffraction under gas pressure.

Polycrystalline samples of **CCP-1** and **CCP-2** were lightly ground in an agate mortar and pestle and filled into a 0.7 mm borosilicate capillary. Data was collected for each sample in the 2θ range 0 – 40 ° on beamline BL04-MSPD at ALBA Synchrotron, Spain, using λ = 0.799332 Å and a Mythen detector comprising 6 modules. The samples were pumped for ca. 30 minutes, after which the gas pressure was increased to 6 bar. The capillaries were allowed for stabilization for 30 minutes before data collection at 295 K. A Rietveld refinement[S5] was undertaken with the program TOPAS,[S4] using as the starting point the structures determined from single crystal data at 240 K for **CCP-1** and **CCP-2** respectively. One gas molecule (CO_2, C_2H_4 or CH_4) was included in the refinement, and refined as a rigid body with rotational and translational freedom. In addition, the occupancies of the gas molecules were also refined, but the displacement parameter was kept fixed. Atomic positions and displacement parameters of the non-hydrogen atoms of the framework were refined subject to a series of restraints on bond lengths, bond angles and planarity of the aromatic rings. The perchlorate and tetrafluoroborate anions were modelled as disorder over two positions, as in the single crystal experiments. A March-Dollase correction of the intensities for preferred orientation was applied in the final stage of refinement. Rietveld refinements converged to R_{wp} = 0.0214, gof = 2.183 in **CO_2@CCP-1**, R_{wp} = 0.0162, gof = 1.919 in **C_2H_4@CCP-1**, R_{wp} = 0.0107, gof = 1.285 in **CH_4@CCP-1**, R_{wp} = 0.0313, gof = 3.271 in **CO_2@CCP-2**, R_{wp} = 0.0357, gof = 3.738 in **C_2H_4@CCP-2**, and R_{wp} = 0.0329, gof = 3.442 in **CH_4@CCP-2**. The observed and calculated diffraction patterns for the refined crystal structures are shown in Figure S3. CCDC-1473649 (**CO_2@CCP-1**), -1473650 (**C_2H_4@CCP-1**), -1473651 (**CH_4@CCP-1**), -1473652 (**CO_2@CCP-2**), -1473653 (**C_2H_4@CCP-2**) and -1473654 (**CH_4@CCP-2**) contain the supplementary crystallographic data for this paper. Figure S4 shows the residual electron density inside the cavity upon increasing CO_2 pressure before inclusion of the gas molecule in the refinement.

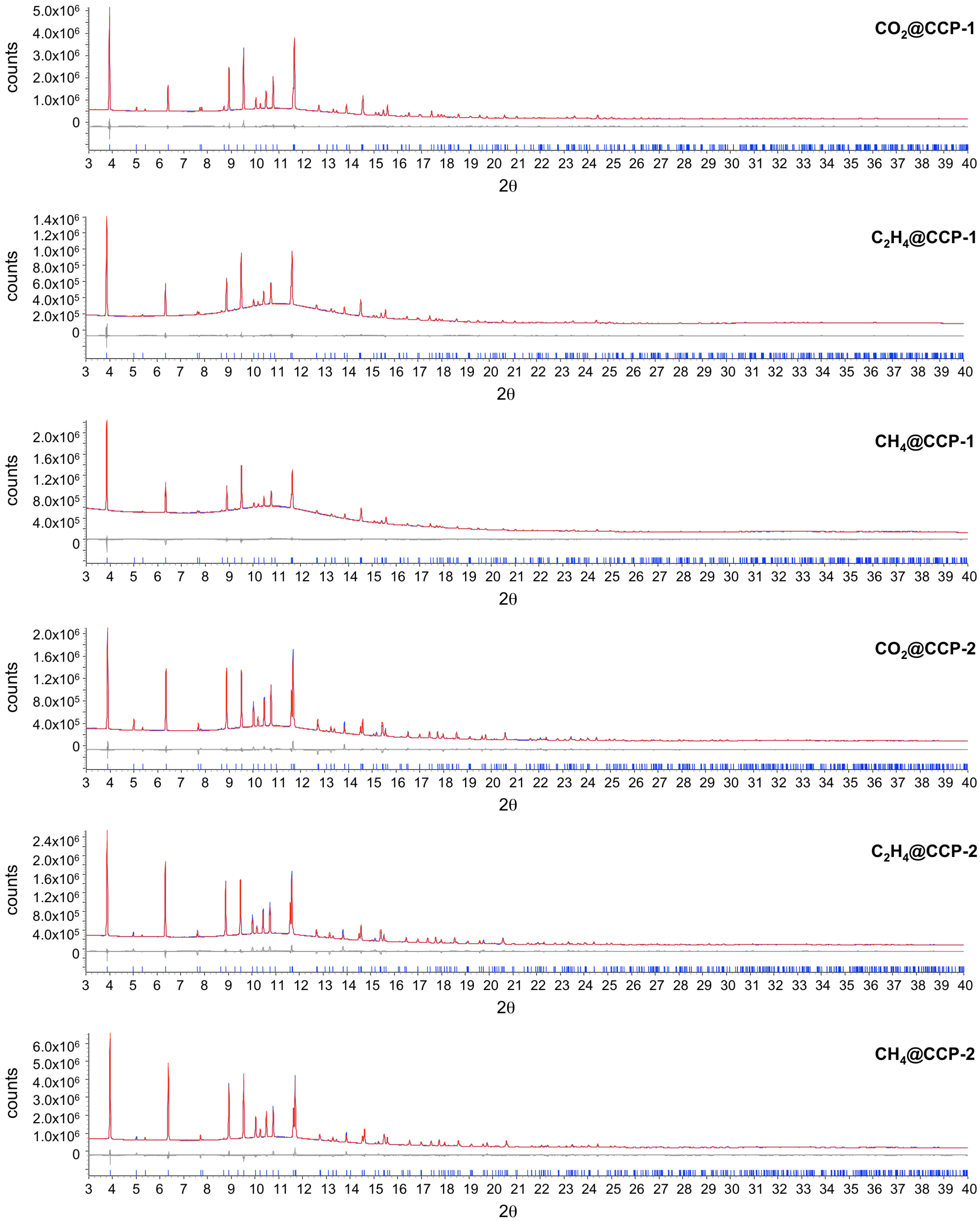

Figure S3. Observed (blue) and calculated (red) profiles and difference plot [(I_{obs} – I_{calcd})] (grey) of the Rietveld refinements for **CCP-1** and **CCP-2** after different gas loadings.

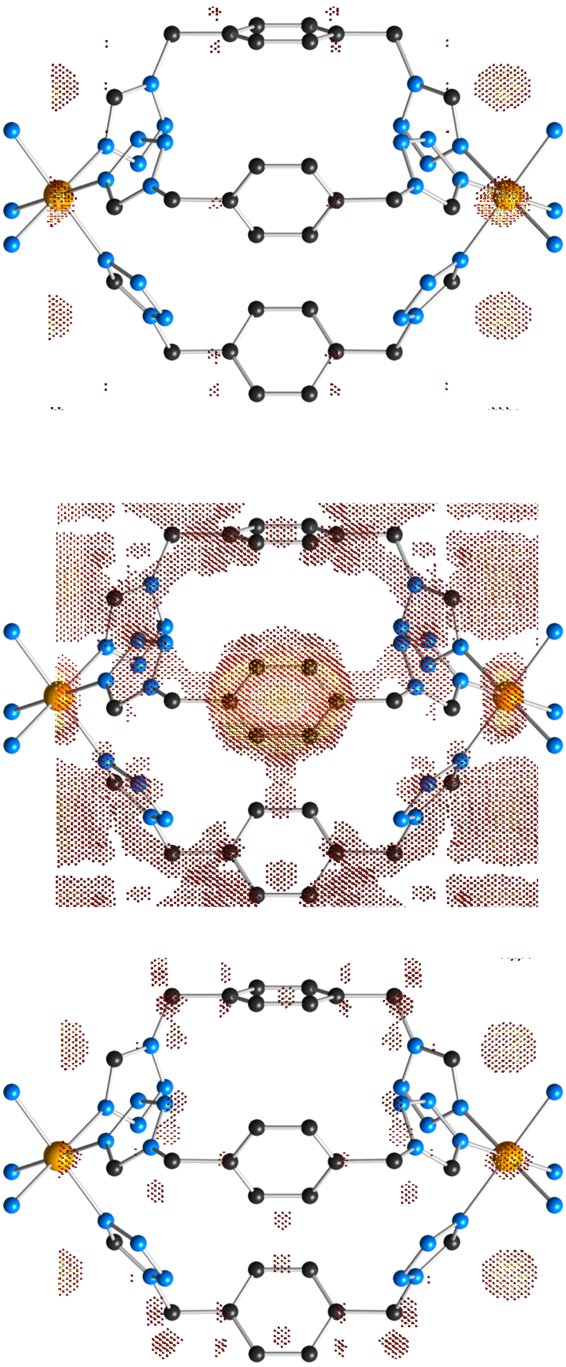

Figure S4. **Top**: residual electron density upon activation of **CCP-1**. **Middle**: residual electron density after increasing the CO_2 pressure to 1 bar, before including in the model the CO_2 molecule. The increase in the electron density inside the cavity is evident. **Bottom**: residual electron density after increasing the CO_2 pressure to 1 bar, after including in the model the CO_2 molecule (not shown for clarity)

S6. Gas sorption studies.

S6.1. Gas sorption isotherms. High-resolution isotherms of CO and C_2H_2 were measured at a series of temperatures in a Micromeritics ASAP 2010 volumetric instrument using approximately 150 mg of sample as a powder. The sample was placed in a sample holder that was immersed into a liquid recirculating thermostatic bath (Julabo FP40-HL) able to control the adsorption temperature from 273 to 333 K with accuracy better than 0.05 K. Prior to adsorption experiments, the sample was outgassed at 423 K for 6 hours under turbomolecular high vacuum. To avoid He adsorption after free space volume determination the sample was outgassed for 1 hour at 423 K prior to gas adsorption.

High pressure CO_2, CH_4, C_2H_6, and C_2H_4 adsorption isotherms and kinetic measurements were performed in an IGA-3 gravimetric analyser (Hiden Isochema). Approximately, 50 mg of sample were placed in the balance. Before each adsorption experiment, the sample was outgassed at 423 K under a final pressure of 10^{-5} Pa during four hours. The temperature of the sample was subsequently reduced under high vacuum until the target temperature (from 283 to 333 K) for each adsorption experiment. Adsorption measurements were performed by introducing gas up to reach the desired pressures. Typically, 16 equilibrium data points up to 800 kPa were recorded for each gas and adsorption temperature in order to build the isotherms. The equilibrium conditions were fixed at the 98 % of the calculated uptake using the Avrami's model or a maximum equilibration time of 120 minutes for each point of the isotherms.

We have applied a virial equation for fitting experimental data points and it was found that a fourth grade polynomial is able to properly describe the isotherms. In some cases, the best fitting of the experimental data was obtained by the Toth equation, as a modification of the Langmuir equation, but including a heterogeneity factor n. Once the experimental data was properly fitted, the heat of adsorption was calculated accordingly to the Clausius-Clapeyron equation from the isotherms taken at different temperatures.

The virial, Toth and Clausius-Clapeyron equations that have been used during the data analysis are given in Table S5.

Table S5. Equations used during the data analysis from the adsorption isotherms

Virial	$\ln\left(\frac{P}{Q}\right) = A_0 + A_1 \cdot Q + A_2 \cdot Q^2 + A_3 \cdot Q^3 + A_4 \cdot Q^4$
Toth	$Q = \frac{Q_{max} \cdot \alpha \cdot P}{\left[1 + (\alpha \cdot P)^n\right]^{\frac{1}{n}}}$
Clausius-Clapeyron	$q_{st} = -R \cdot \left[\frac{\partial(\ln P)}{\partial\left(1/T\right)}\right]_{Q=cte}$

Table S6. Physical properties of the different gases used in this study.[S6,S7]

	CO_2	N_2	CH_4	ethane	ethylene	acetylene	CO
Kinetic diameter [Å]	3.30	3.64–3.80	3.758	4.443	4.163	3.30	3.69
Quadrupolar moment x 10^{26} [esu·cm^2]	4.30	1.52	0	0.65	1.50	6.03	2.50
Polarizability x 10^{25} [cm^3]	29.11	17.403	25.93	44.3–44.7	42.52	33.3–39.3	19.5
Dipole moment x 10^{18} [esu·cm]	0	0	0	0	0	0	0.1098

CO_2

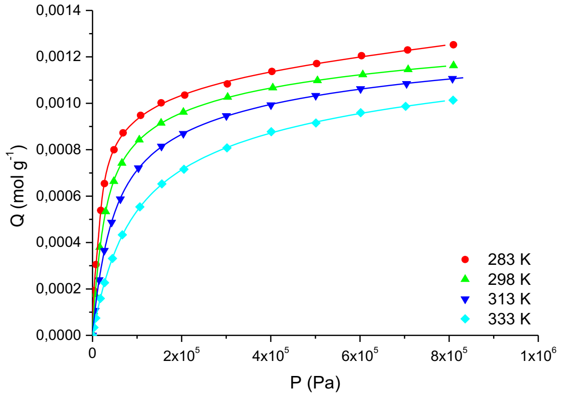

CH_4

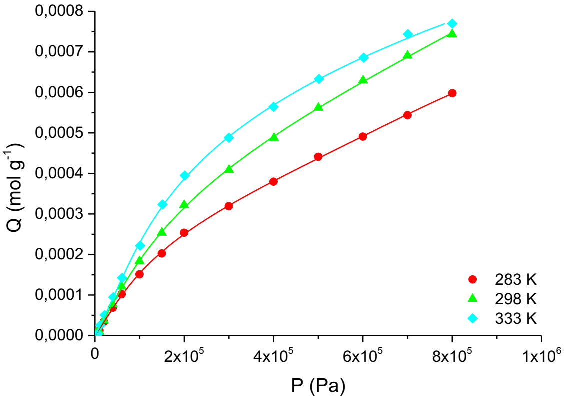

CO

C_2H_6

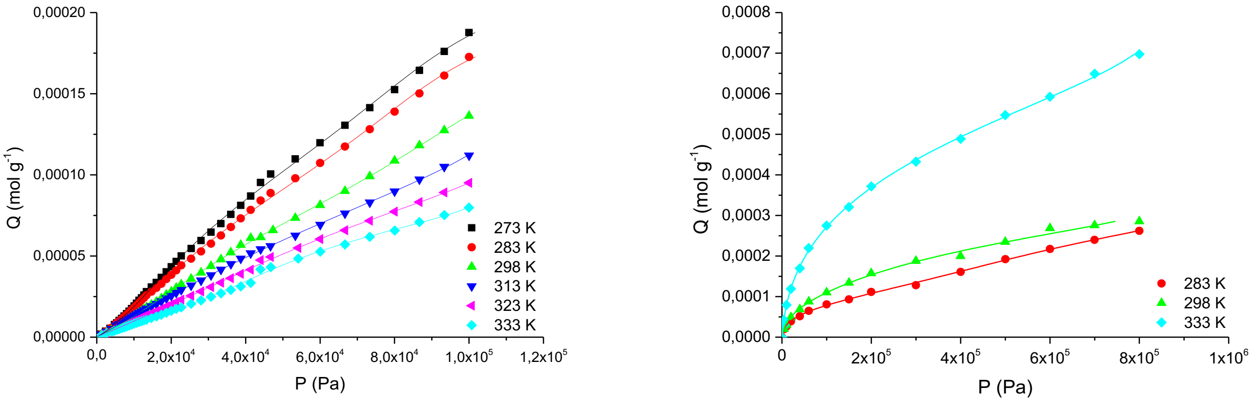

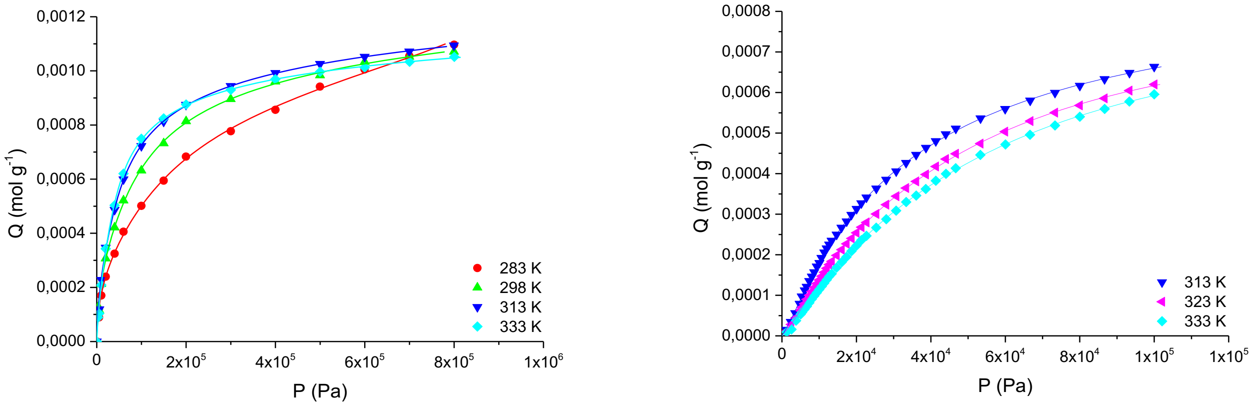
C$_2$H$_4$

C$_2$H$_2$

Figure S5. Gas adsorption isotherms (mol g^{-1}) for different gases at different temperatures for **CCP-1**. Lines correspond to virial fits.

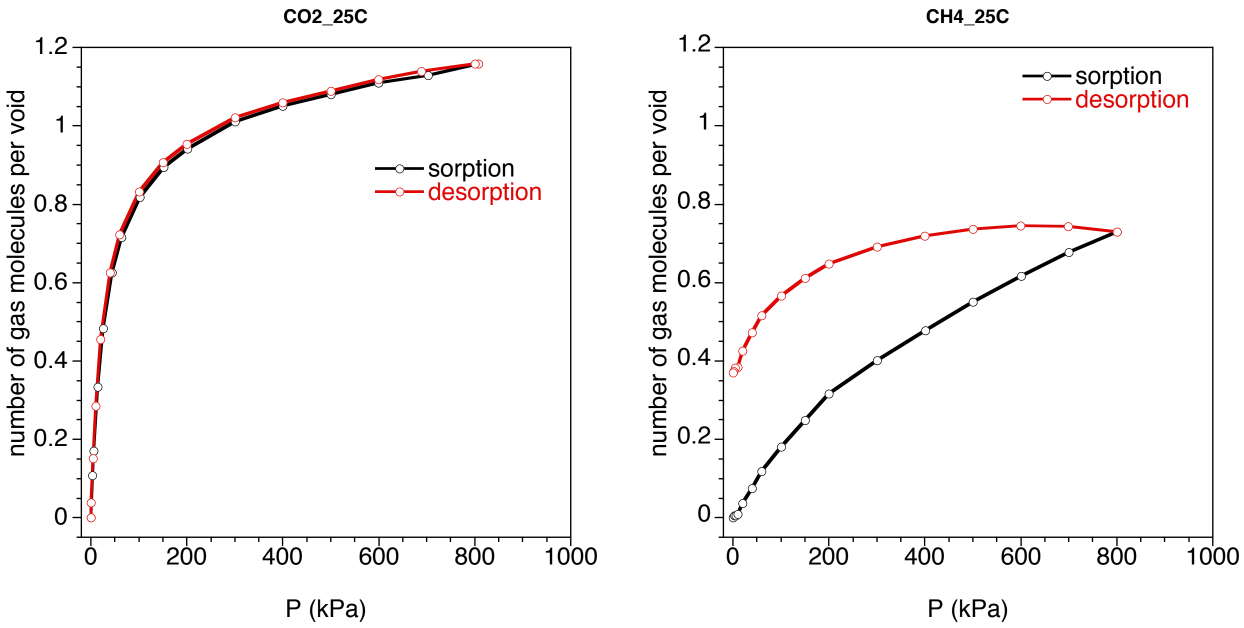

Figure S6. Adsorption/desorption isotherms for CO_2 and CH_4 at 298 K for **CCP-1**. The hysteresis observed for CH_4 further confirms the diffusion problems.

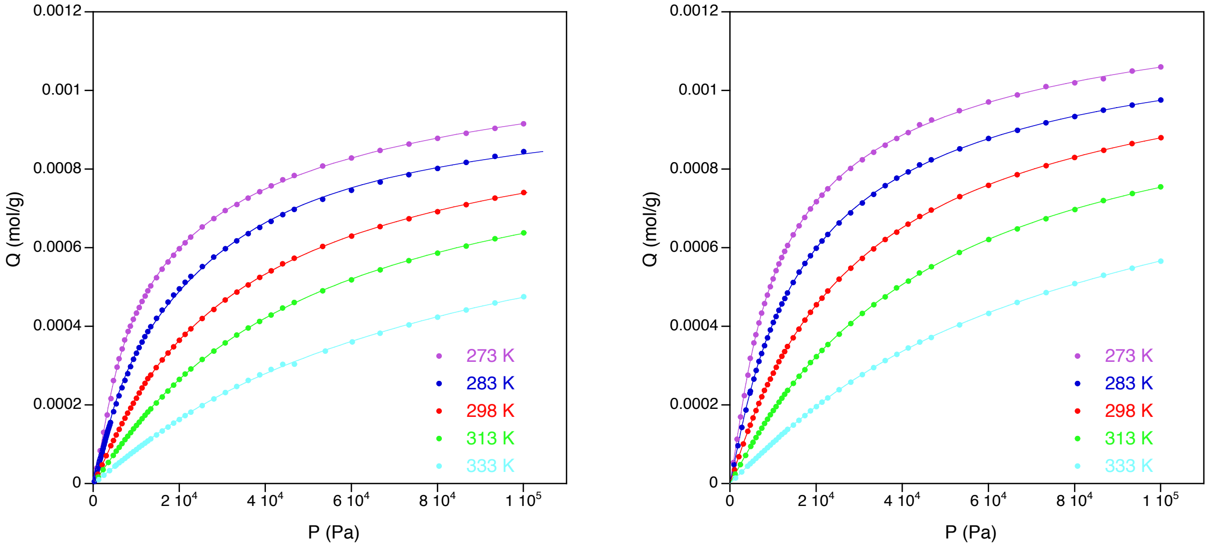

(a) (b)

Figure S7. Low pressure adsorption isotherms collected at different temperatures of CO_2 on **CCP-1** (a) and **CCP-2** (b). Lines correspond to the best fits. Virial equation was used in (a) and (b), Toth equation in (c) and (d).

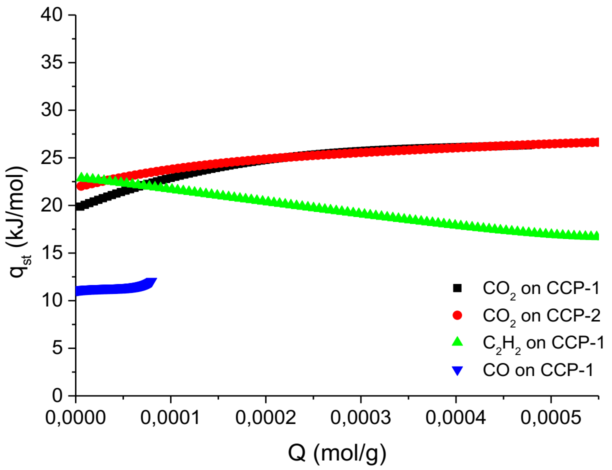

Figure S8. Isosteric heats of adsorption.

S6.2. Kinetic study. The kinetic experiments were performed in an IGA-3 gravimetric analyser (Hiden Isochema). Approximately 50 mg of the adsorbant were outgassed in the balance at 423 K under high vacuum prior the kinetic study. Next, the sample was cooled down to the analysis temperature, 298 K. Then, the pressure was raised up to 30 kPa and the weight gain was recorded as a function of time for 12 hours.

The diffusion ability of the gases was measured in terms of its characteristic D_c/r_c^2 values, where D_c is the Fickian diffusion coefficient and r_c is the averaged radius representative of the crystal size distribution of the adsorbant. D_c/r_c^2 can be derived from adsorption kinetic measurements by using the solution to spherical particles of the equation described by Crank:[S8]

$$\frac{Q}{Q_{max}} = 1 - \frac{6}{\pi^2} \sum_{n=1}^{\infty} \frac{1}{n^2} \exp\left(- \frac{n^2 \pi^2 D_c t}{r_c^2} \right)$$

where Q represents the gas uptake at a time t and Q_{max} the uptake at the equilibrium. For the fitting, the 20 first members of the series were used, because they decay exponentially and converge to zero.

Table S7. D_c/r_c^2 values for the four gases measured.

	D_c/r_c^2	Ratio with CO_2
CO_2	$1.297 \cdot 10^{-4}$	-
methane	$3.033 \cdot 10^{-6}$	42.8
ethane	$3.136 \cdot 10^{-6}$	41.4
ethylene	$3.128 \cdot 10^{-6}$	41.5

S6.3. Binary breakthrough measurements. Breakthrough curves of binary gaseous mixtures were carried out on a homemade instrument, illustrated in Scheme S1. In all cases, the sample was pelletized and sieved between 0.2 and 0.4 mm. The solid adsorbent was loaded into a stainless steel tubular column of 6.0 mm internal diameter, with quartz wool as filler. The weight of adsorbent was 1.2375 g, with a length of 13.5 cm inside of the aforementioned column. The gaseous flows were adjusted by using calibrated mass-flow controllers (Iberfluid Instruments) so, different feed compositions could be studied. The total feed flow was maintained at 40 ml/min in all cases. The gaseous mixture could be sent into the packed column of adsorbent, or by-passed by using a 6 port valve (Valco). The same valve was also used for feeding helium to the column during the degasification process at high temperature. The column was heated by means of an electric mantle, and the temperature was controlled during the experiments with a thermostatic bath (Julabo F25) connected to the double-jacketed column. Prior to the breakthrough experiments, the adsorbent was activated at 353 K in 40 ml/min of helium for two hours. The reactor was then cooled down to 298 K before switching to the gas mixture. Both the by-pass and the stream from the column can be sent to vent or to analyze through two different 4 port valves (Valco). The pressure in the column and the by-pass line was regulated by two different electronic pressure gage controllers (Bronkhorst). One particularity of the setup is the use of a mass flow meter based in the Coriolis effect (Bronkhorst) connected downstream the column. The Coriolis flow meter provide with a value of the mass flow in g/h. Also, the composition of the exhausted gas was monitored with a mass spectrometer. The total flow together with its composition could be calculated by combining the calibrated Coriolis flow meter and the mass spectrometer.

The adsorption selectivity was defined as the ratio of the two adsorbed gases under specific conditions of pressure and temperature, given by the following equation[S9]:

$$\alpha_{ij} = \frac{x_i}{x_j} \cdot \frac{y_j}{y_i}$$

Where $x_{i/j}$ are the adsorbed amounts of components i and j at equilibrium from a gas mixture of defined by the molar fractions $y_{i/j}$. The adsorption selectivity can be obtained in terms of molar flow of the adsorbed gases according to the equation

$$\alpha_{ij} = \frac{F_{i,0} \int_0^{t_\infty} \left(1 - \frac{F_i}{F_{i,0}}\right) dt}{F_{j,0} \int_0^{t_\infty} \left(1 - \frac{F_j}{F_{j,0}}\right) dt} \cdot \frac{y_j}{y_i}$$

Being F_i and F_j the molar fluxes of components i and j respectively during the breakthrough experiment, and $F_{i,0}$ and $F_{j,0}$ the molar fluxes of components i and j in the feed stream. The dead volume was determined by flowing helium though the saturated column and subtracted for the calculation of the adsorbed amount of each specie.

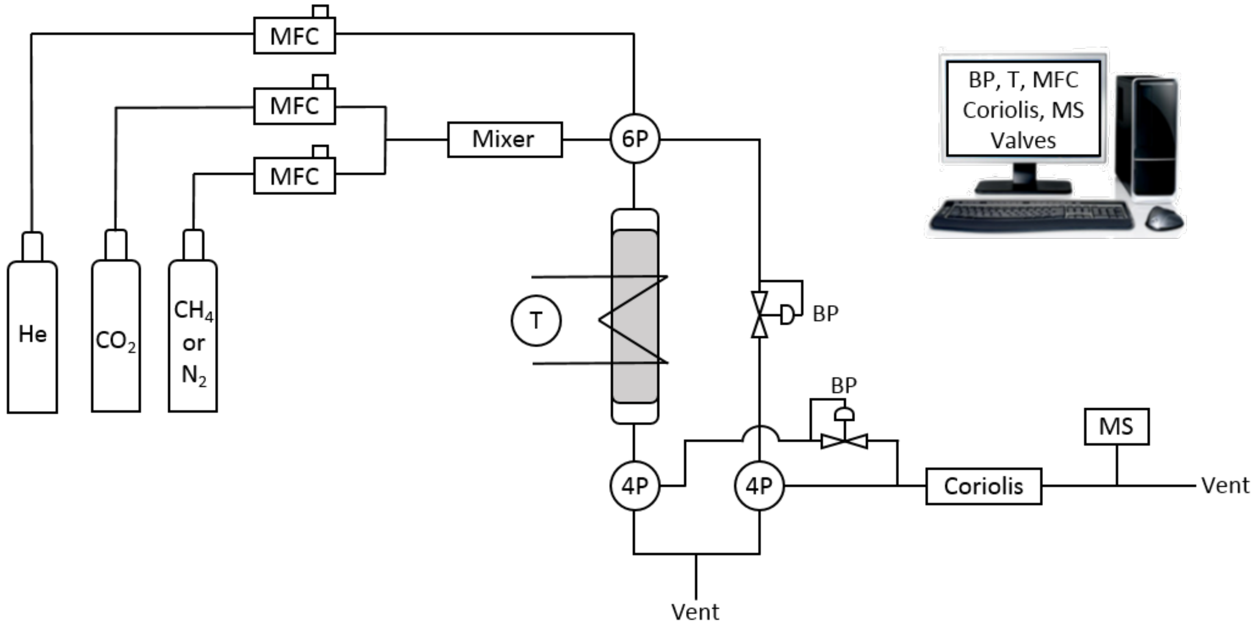

Scheme S1. Schematic diagram of the breakthrough apparatus used for binary adsorption. MFC, mass flow controller; 6P, 6 port valve; 4P, 4 port valve; BP, pressure controller; T, temperature control (heating mantle or recirculated bath); MS, mass spectrometer.

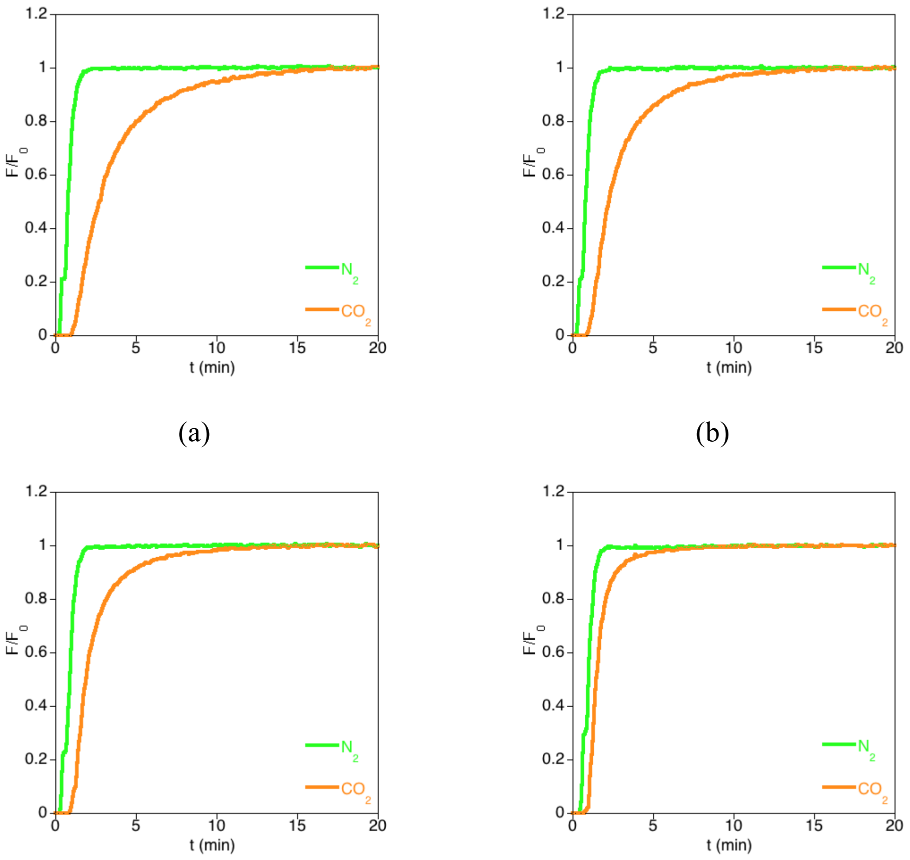

(a)

(b)

(c)

(d)

Figure S9. Binary breakthrough experiments for different mixtures of CO_2 and N_2 at 298 K and 2 bar for **CCP-2**. a) CO_2:N_2 5:95. b) CO_2:N_2 10:90. c) CO_2:N_2 20:80. d) CO_2:N_2 50:50.

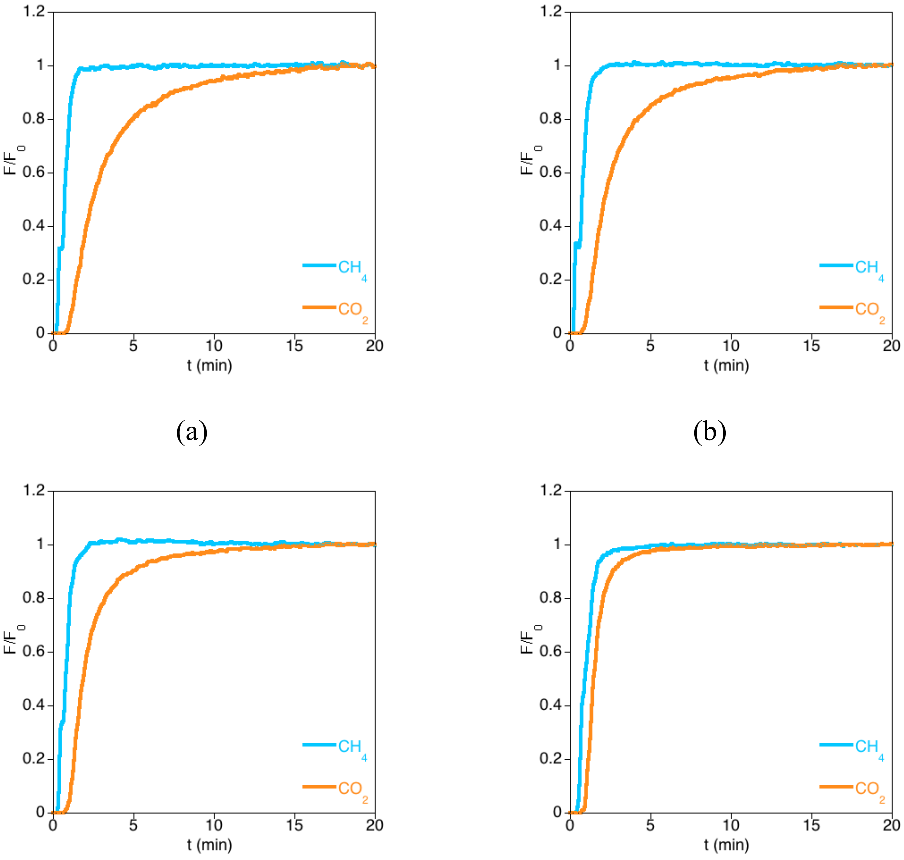

(a) (b)

(c) (d)

Figure S10. Binary breakthrough experiments for different mixtures of CO_2 and CH_4 at 298 K and 2 bar for **CCP-2**. a) CO_2: CH_4 5:95. b) CO_2: CH_4 10:90. c) CO_2: CH_4 20:80. d) CO_2: CH_4 50:50.

S7. Magnetic measurements.

Magnetic susceptibility measurements were carried out on single-phased polycrystalline samples with a Quantum Design MPMS-XL-5 SQUID susceptometer. The susceptibility data were all collected at 1 K·min^{-1}, with an applied field of 0.1 T for **CCP-1** and **CCP-2** and the gas loaded systems. Magnetic susceptibility measurements of the gas loaded systems were performed by sealing a glass tube with 10 mg of **CCP-1** and **CCP-2** and a known amount of the gas (CO_2, CH_4, C_2H_6, C_2H_4, CO, propane, N_2, N_2/CO_2) or after heating a loaded sample to remove the CO_2 molecules. Prior to the gas loading, the samples were activated by heating in situ at 150 °C for 3 h under vacuum.

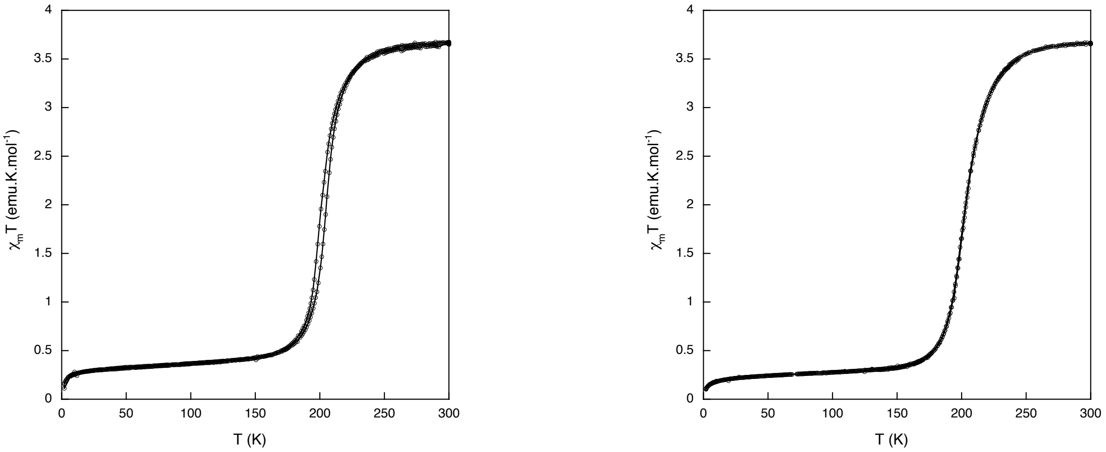

(a) (b)

Figure S11. Temperature dependence of χ_MT for **CCP-1** (a) and **CCP-2** (b) in the temperature range 2–300 K at 0.1 T.

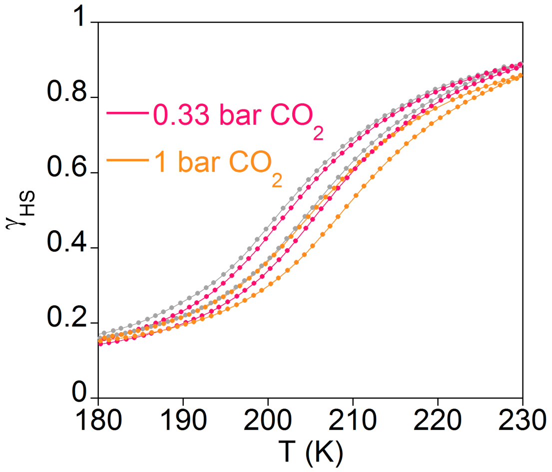

Figure S12. Detailed view of the spin transition region of **CCP-2** upon partial loading of CO_2.

S8. Scanning Electron Microscopy

Crystallite morphologies and dimensions were studied with a Hitachi S-4800 field emission scanning electron microscope at an accelerating voltage of 10 kV with metallization of the samples.

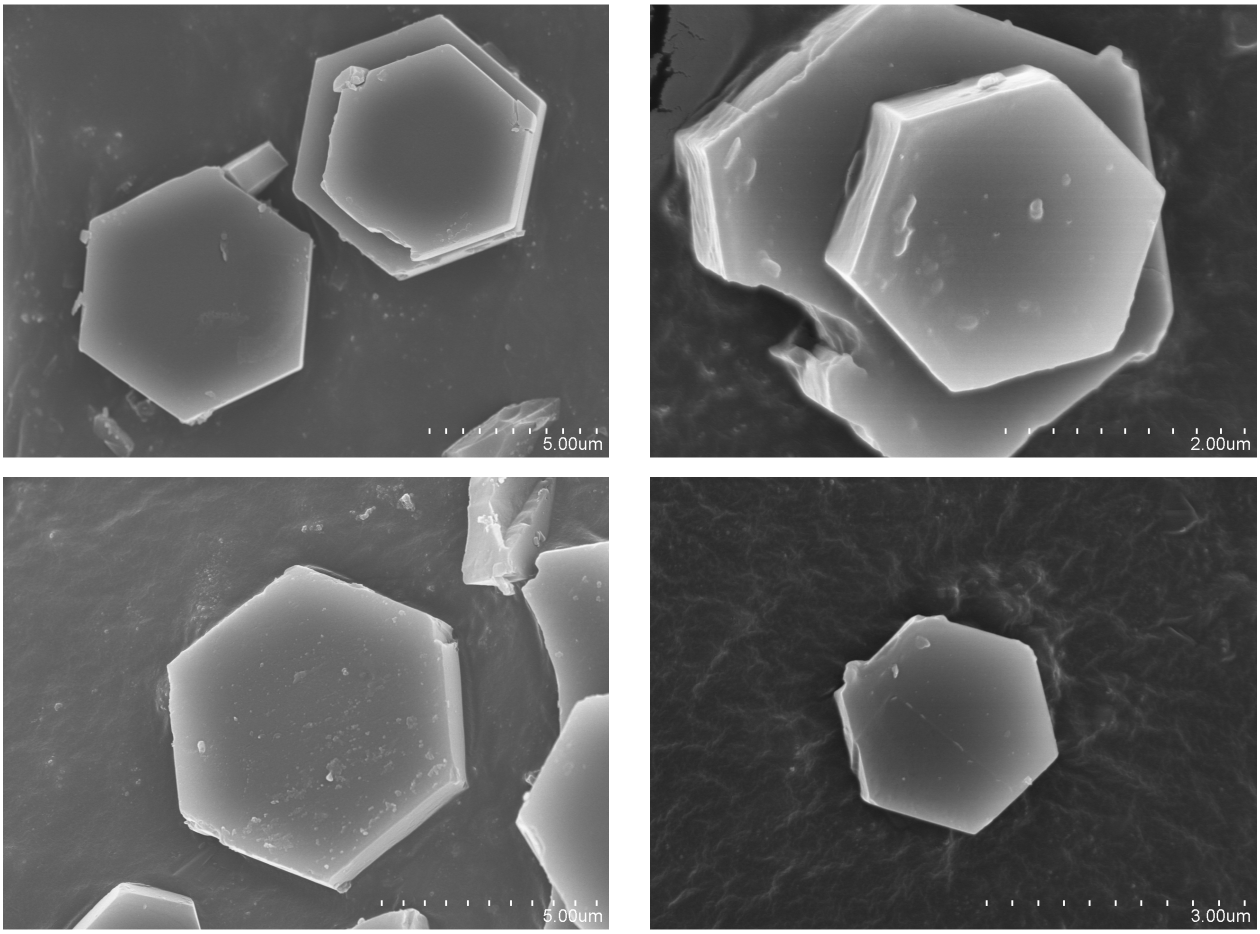

Figure S13. Different SEM images of **CCP-1**.

S9. Inelastic Neutron Scattering.

S9.1. Experimental setting. The Inelastic Neutron Scattering (INS) spectra was measured at 5 K in the range of energy transfers from 16 to 4000 cm^{-1} with and energy resolution of $\Delta E/E \approx 2$ using LAGRANGE, the neutron vibrational spectrometer installed at the hot source of the high-flux reactor at the Institute Laue-Langevin in Grenoble. The primary spectrometer consists in a new large double-focusing multi-face crystal monochromator supplying monochromatic beam in the intermediate and high neutron energy ranges (mosaic Cu220 and Cu331 crystal faces) as well as in the lower energy range (elastically bent Si111 and Si311 reflections). The secondary spectrometer is based on the space focusing of neutrons scattered by the sample in a very large solid angle, which are all then recorded with a relatively small single counter (a He3 gas detector). The focusing reflecting surface of ~1 m^2 is built around the vertical sample-detector axis from pyrolytic graphite (PG) crystals set to reflect neutrons with the fixed average energy of 4.5 meV. It is important that the requested energy resolution of the instrument is achieved with a relatively low grade of the pyrolytic graphite. The appropriately shaped beryllium filter is installed immediately after the sample in order to remove higher-order harmonics in the analyzer reflections. The whole instrument can be considered as a variant of a classical three-axis spectrometer with a very large barrel-like fixed-energy analyzer.

In the present experiment the energy transfer was calculated by subtracting 4.5 meV, the energy of the PG crystals in the ellipsoid, from the energy of the incoming neutrons selected with a focusing Cu(220) single crystal and bent Si(111) and Si(311) reflections.

The background spectrum from the cryostat and an empty sample holder was measured separately and then subtracted from the raw INS spectrum of the sample. In the extent that k_f is much smaller than k_i, the observed intensity is directly proportional to the generalized density of states (GDOS), that is the hydrogen partial density of states in the case of hydrogenated materials. Data sets were then normalized for monitor counts and corrected for empty cell. The sample was placed in an Al cell connected to the gas injection stick. The aluminium cell was placed inside a cryostat allowing a precise temperature control.

S9.2. Brief introduction of the technique. Among vibrational spectroscopies, Inelastic Neutron Scattering (INS) presents very specific features. First, this technique is mainly sensitive to vibrations involving hydrogen atoms because of their much higher incoherent cross-section as compared to other elements. Second, neutrons can only properly be described as quantum mechanical entities; thus, they exhibit both wave-like and particle-like properties, and for that reason an inelastic scattering event results in a significant transfer of both energy (E, cm^{-1}) and momentum (Q, Å^{-1}). The energy transfer (E_T) is given by: $E_T = E_i - E_f$, where the subscripts *i* and *f* refer to the incident and final values, respectively. The momentum transfer is given by: $\mathbf{Q} = \mathbf{k_i} - \mathbf{k_f}$, where $\mathbf{k} = 2\pi/\lambda$, **k** is the wavevector; λ is the wavelength of the neutron.

INS spectroscopy spans a wide range in energy, with energies ranging from that of the microwave region to the ultraviolet region of the electromagnetic spectrum, but in this study we restrict ourselves to energy transfers equivalent to that of the infrared region, 0–4000 cm^{-1}.

In the case of Raman and IR scattering processes the momentum transfer are $Q \approx 0$ and therefore both techniques are subjected to the selection rule that only transitions at zero wavevector are observable.

For the reasons explained above Inelastic Neutron Scattering (INS) is a highly powerful technique for studying the lattice dynamics and atomic and molecular vibrations in materials, especially those containing light elements as hydrogen. INS allows measuring the generalised Density of States (GDOS) of a powder sample, which is a particularly useful quantity for studying lattice dynamics. This is particularly useful for a direct comparison with simulation data.

The observed quantity in a neutron experiment is proportional to the double differential cross section:

$$\frac{\partial^2\sigma}{d\Omega dE} = \left(\frac{\partial^2\sigma}{d\Omega dE}\right)_{coh} + \left(\frac{\partial^2\sigma}{d\Omega dE}\right)_{inc},$$

which gives the number of neutrons scattered by the sample into a solid angle $d\Omega$ around Ω, with a final energy included between E–dE and E+dE. The total intensity and the relative proportion between coherent and incoherent depends on the specific chemical composition of the sample. Hydrogen atoms have the largest, and mostly incoherent, scattering cross section. In this case, when performing INS experiment on hydrogenated structures, the neutron spectra will be dominated by the incoherent contributions of the H atoms.

The form of the double differential scattering cross section can be rewritten in terms of a function S, which emphasises the dynamics of each individual atom in the sample. This is conventionally called the scattering law and is directly related to the observed intensities when summed over all the atoms in the sample:

$$S(\vec{Q},\omega)_l = \frac{4\pi}{\sigma_l}\frac{k_i}{k_f}\left(\frac{\partial^2\sigma}{d\Omega dE}\right)_l,$$

where *l* refers to one specific atom of the molecule.

The main significance of the scattering law is that it is the natural meeting point of experimental data and the dynamical simulated models that have been developed for its understanding. The calculated relative intensity of the i^{th} mode determined at a momentum transfer $\vec{Q}$ and at an energy transfer ω_i, *S* of an INS band is given by:[S10]

$$S(Q, n\omega_i) \propto \frac{(QU_i)^{2n}}{n!} \exp\left[-(QU_{Tot})^2\right] \sigma$$

,

where ω_i is the i^{th} mode at frequency ω, n=1 for a fundamental, 2 for a first overtone or binary combination, 3 for a second overtone or ternary combination, etc., *Q* is the momentum transfer defined above, U_i is the root mean square displacement of the atoms in the mode, and σ is the inelastic cross section of the atom. The exponential term in the expression shown above is the Debye-Waller factor, U_{Tot} is the root mean square displacement of all atoms in all the modes, and its magnitude is in part determined by the thermal motion of the molecule. The intensities of the features in a neutron spectrum depend then on the amplitude of the vibrations of each atoms involved in a particular mode weighted by their scattering power σ_i/M_i, where σ_i and M_i are the scattering cross section and the mass of the atom *i* respectively. The Generalized Density of states (GDOS) $G(\omega) \approx \sum_i \sigma_i/M_i \cdot g_i$ obtained from an INS experiment differs from the real vibrational density of states (VDOS) that can be calculated by normal modes analysis and *ab-initio* molecular dynamics simulations.

S10. Computational details

S.10.1. Normal modes calculation. The theoretical VDOS(ω) was calculated using the direct method on the basis of first-principles calculations. Calculations of the relaxed structure and the eigen modes, obtained from the dynamical matrix, were calculated by using the DMol3 *ab-initio* simulation package in Materials Studio software[S11] package using the GGA PBE functional[S12] with the DND basis set. Experimental lattice parameters were fixed in the calculation to the experimental ones and only the atomic positions were relaxed. All electronic functions and the dynamical matrix were calculated at the Γ- point.

The Vibrational Density of states (VDOS) is calculated from the partial density of states, g_i, of the different atomic species: VDOS(ω) ~ $\Sigma_i\ g_i$.

The calculated INS spectra (GDOS) were calculated for the bare MOF using the aClimax software.[S13] Figure S14 shows the comparison of the experimental and the calculated INS spectra that is docomposed in the different contributions, the fundamental vibrations modes (n=1) and the first overtone (n=2) and the comparison with the experimental results. Taking into account the overtones on the calculated INS spectra, it can be clearly seen that the vibrational spectra can be fully described.

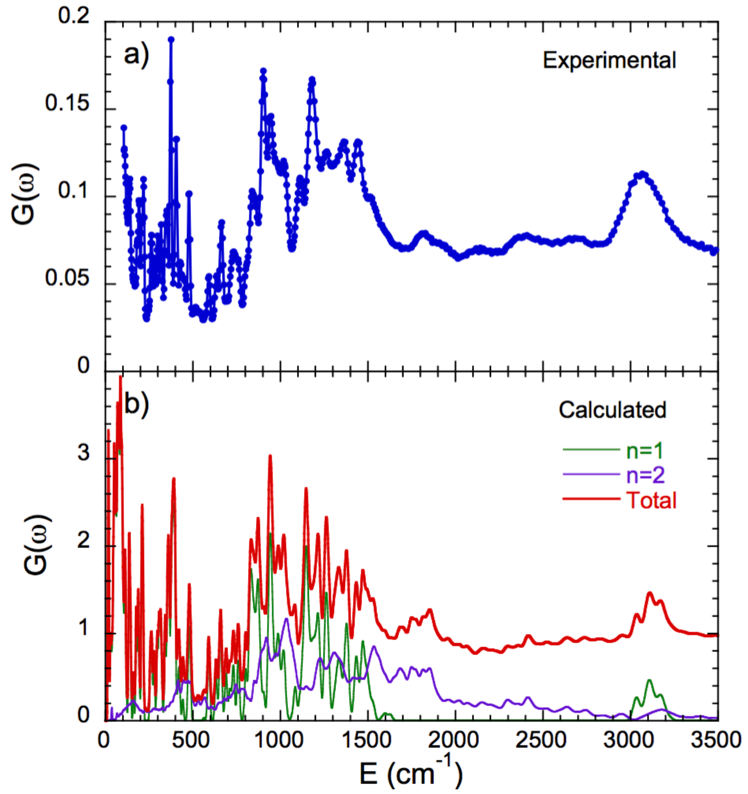

Figure S14: a) Experimental results of the bare MOF and b) INS spectra calculated using DMol3 in Materials Studio and generated using the software aClimax.

Table S8. Assignment of selected vibrational bands of **CCP-1**.

DMol3 Frequency / cm^{-1}	***Nature of Vibration***
360.0	Sp^3 C-H bend
422.0	Sp^3, Phenylene, Tetrazole C-H bend
657.0	Tetrazole C-H bend
865.5	Sp^3, Phenylene, Tetrazole C-H bend
931.3	Sp^3 C-H bend
1159.8	Phenylene C-H bend
1197.9	Phenylene C-H bend
1346.8	Sp^3 C-H bend
1433.3	Sp^3 C-H bend

S.10.2. ***Ab-initio*** **Molecular Dynamics Simulations.** Traditionally, Molecular Dynamics (MD) simulations use (semi) empirical interatomic potentials, allowing nowadays to treating efficiently large scale structures and macromolecules systems. In DFT-MD the atoms are moved according to classical Newton's mechanics but the interatomic forces acting between the atoms are computed according to quantum mechanics, solving from first- principles the electronic structure for a given set of atomic positions and then calculating the resulting forces on each particle. In this case, the vibrational spectra can be extracted from MD trajectories, via the Time Fourier Transform of the velocity-velocity autocorrelation function:

$$g(\omega) = \sqrt{\frac{1}{2\pi}} \int_{-\infty}^{\infty} e^{i\omega t} \sum_i \frac{\langle \vec{v}_i(t)\vec{v}_i(0)\rangle}{\langle \vec{v}_i(0)\vec{v}_i(0)\rangle} dt$$

where the function $\frac{\langle \vec{v}_i(t)\vec{v}_i(0)\rangle}{\langle \vec{v}_i(0)\vec{v}_i(0)\rangle}$ is the velocity-velocity autocorrelation function (VAF), calculated from a chosen initial time (t=0) for the MD trajectory and for each atom of the system i, along all three components of the velocity $\vec{v}_i$. The DFT calculations were performed using the VASP code.[S15]All calculations use optimised norm-conserving pseudopotentials generated with the Perdew-Burke-Ernzerhof (PBE) functional within the generalized- gradient approximation (CGA). Optimized structures were used as input for the production of molecular dynamics (MD) trajectories. They MD simulations were performed at 300K in the NVT ensemble over 20 ps with a 1 fs timestep. DOS was computed as time-Fourier transform of the velocity autocorrelation function (VACF) computed from the coordinates of each step of the trajectories, as implemented in the nMOLDYN program.[S15]

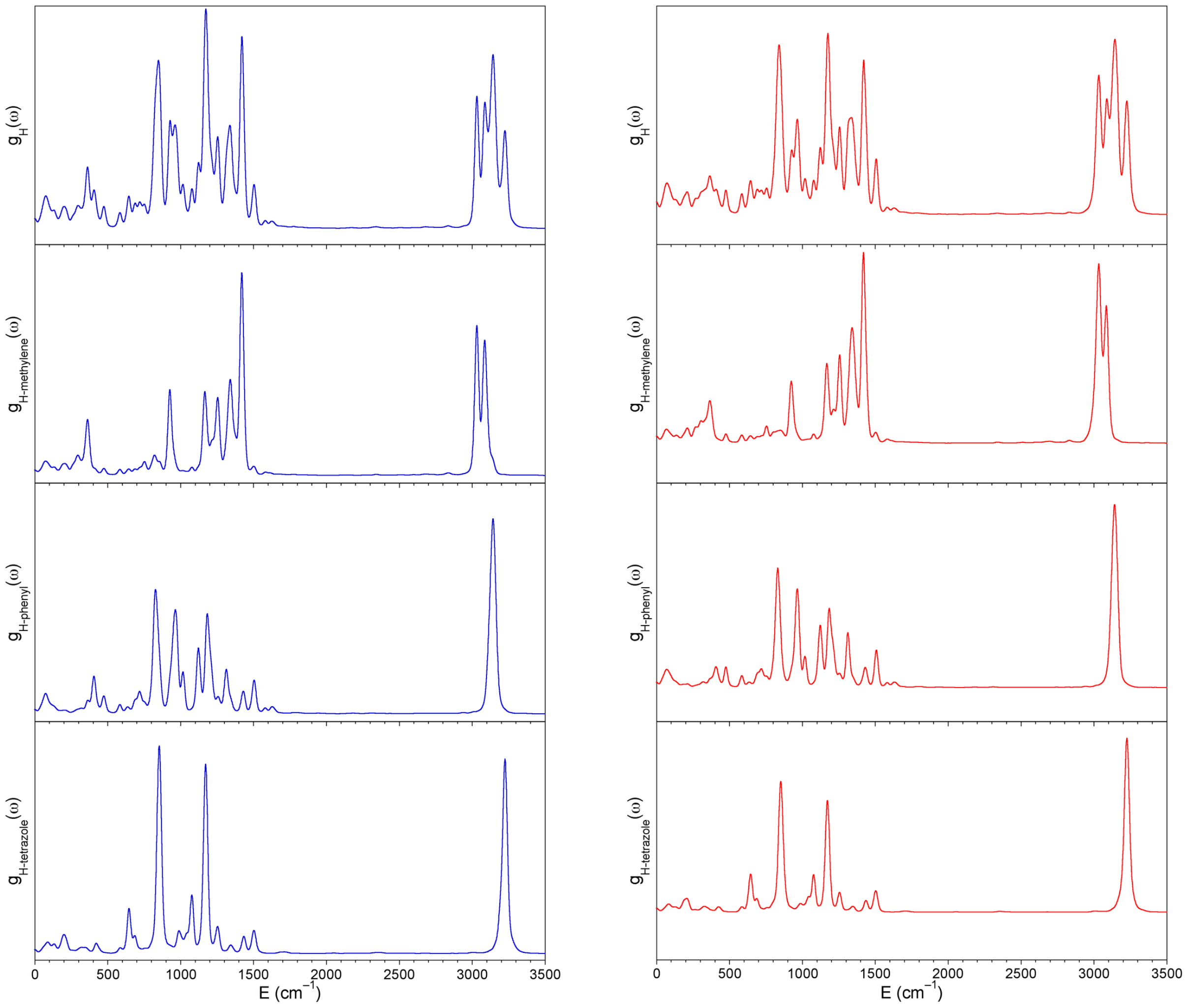

Figure S15. Comparison of the calculated H partial density of states, $g_H(\omega)$, $g_{H\text{-methylene}}(\omega)$, $g_{H\text{-phenyl}}(\omega)$ and $g_{H\text{-tetrazole}}(\omega)$ for the bare **CCP-1** (left) and **CCP-1** loaded with CO_2 (right).

S11. Quasielastic Neutron Scattering

QENS experiments were performed in the direct time-of-flight spectrometer IN5 at the Institut Laue-Langevin (ILL, Grenoble, France) using two different incident neutron wavelengths: λ=5 Å, giving an energy resolution of 0.1 meV (FWHM) and a Q-range of 0.2–2.2 Å^{-1}, and λ=8 Å, resulting in a resolution of 0.25 meV and a Q-range of 0.2-1.4 Å^{-1}. The sample was placed inside a cylindrical aluminium sample holder allowing the gas injection, and temperature control was achieved using a standard ILL orange cryostat. Bare and CO_2-loaded **CCP-1** was measured at 10 selected temperatures between 10 K and 320 K, with acquisition times of 1 hour. For the measurement of the CO_2-loaded compound, the samples were saturated with CO_2 by injecting gas at 900 mbar at room temperature and then cooled while keeping the gas pressure constant. The CO_2 uptake was checked by its effect in the Bragg peaks (see below). Additionally, the empty sample holder and a vanadium sample were measured and used to subtract the background and correct for detector efficiency by applying the standard correction procedures using LAMP. Corrected I(2θ,ω) data were then transformed into I(Q,ω) and rebinned into 22 groups with Q_{min} = 0.2 Å^{-1}, Q_{max} = 2.3 Å^{-1}, and a step of 0.1 Å^{-1}.

The incoherent scattering cross section of hydrogen is significantly larger than the scattering cross sections of the remaining elements present in the system (that scatter mainly coherently), so the signal measured is dominated by the incoherent scattering from H, which represents 81% of the total scattering. However, as the coherent scattering is concentrated in intense Bragg peaks, it is not completely negligible. This is clearly seen in Figure S17, which shows the analogous of the diffraction pattern obtained by integrating the I(Q,ω) data over the whole energy range. The relatively flat contribution decreasing smoothly with Q is due to the incoherent scattering from H, while the sharp peaks contain the coherent contributions of the remaining elements. The decay with Q of the incoherent signal is due to the Debye-Waller factor, $\exp(-u(T)^2Q^2/6)$, where u(T) corresponds to the average vibrational amplitude of the H atoms at temperature T.

Figure S17 also demonstrates that the presence of CO_2 in the voids has a clear effect in some of the Bragg peaks whose intensity is reduced after the loading process. This can be understood at least qualitatively as an effect of a reduced contrast between the scattering lengths of the framework and the cages due to the presence of the gas molecules.

In order to minimize the coherent contamination of the incoherent signal due to H, the detectors corresponding to the more intense Bragg peaks were removed before transforming and rebinning into constant Q. The resulting I(Q, ω) spectra were then fitted by the following model-independent expression:

$$I(Q,\omega) = C(Q)\times [A_0(Q)\delta(\omega) + (1 - A_0(Q))\times L(\Gamma(Q))] + B(Q)$$

where C(Q) is a scaling constant that takes also into account the Debye-Waller factor, B(Q) the remaining background (including also a possible inelastic contribution assumed to be flat in the quasielastic region), $A_0(Q)$ is the elastic incoherent structure factor (EISF), and L(Γ(Q)) a lorentzian function of half-width half-maximum Γ(Q). The EISF is related to the region of space accessible to the scatterers, so its Q-dependence can inform on the geometry of the motion observed by QENS.[S16] In the present case, it will also contain contributions from all the hydrogens of the framework that are fixed.

Figure S16 (top) compares the spectra obtained at 250 K and Q = 1.2 $Å^{-1}$ for the system with and without CO_2 using the best resolution available. No clear differences can be seen, although it seems that the intensity at the bottom of the elastic peak is slightly larger in the loaded system. This could be tentatively attributed to a weak quasielastic signal associated to a fast diffusion of CO_2 inside the framework. Unfortunately the contribution of the scattering cross section of CO_2 to the total is too feeble to allow us to extract any information.

Figure S16 also shows that the intensity of quasielastic scattering is almost negligible compared to the elastic intensity, making the EISF very close to 1 for all the Q values. Assuming that the 12 H atoms attached to phenyl rings move with the ring to allow the diffusion of the gas, while the rest just vibrate around their equilibrium positions, a decay of $A_0(Q)$ to a value of ~0.6-0.8 at high Q could be expected (the exact value depending on the exact type of motion). The present result is therefore an indication that at a given time only a tiny fraction of the phenyl rings is actually moving.

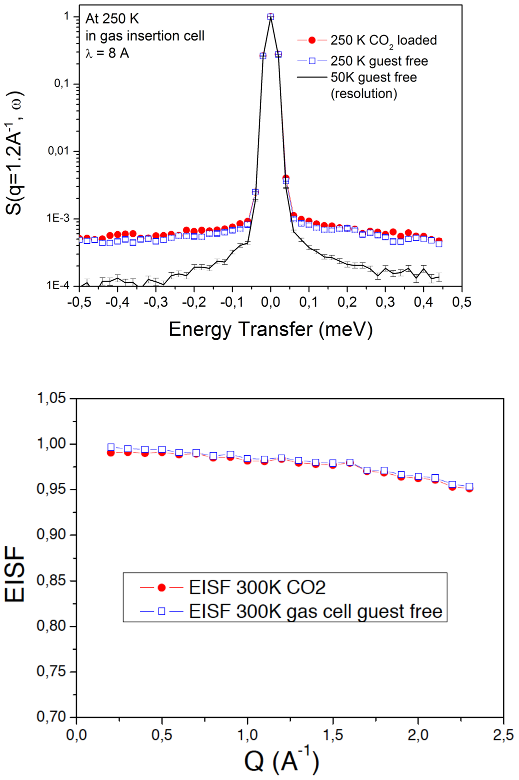

Figure S16. (**top**) QENS spectra for bare **CCP-1** and **CCP-1** loaded with CO_2 at 250 K. The spectrum of bare **CCP-1** at 50 K is also given, as an estimate of the resolution. (**bottom**) Elastic Incoherent Structure Factor (EISF) with and without CO_2 molecules.

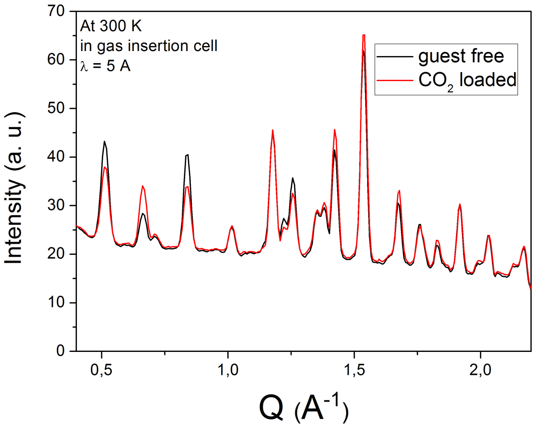

Figure S17. Neutron diffraction powder pattern for bare **CCP-1** (in black) and **CCP-1** loaded with CO_2 (in red) at 300 K and λ = 5 Å, obtained from spectra of the QENS experiments. The difference in peak intensity is related to CO_2 inclusion.

S12. Molecular dynamics study of CO_2 diffusion in CCP-1.

The supercell used for the calculations is a 2×2×1 supercell that contains 760 atoms (a = b = 21.4 Å, c = 23.7 Å). The supercell (see Figure S18) contains cavities (labelled 'X' in the figure) which are shown as blue circles, and it also contains a narrow cavity (labelled 'Y', smaller green circle) which connects with three large cavities as shown in the figure. Neither of the cavities is spherical.

Cavities 'X' can allocate two CO_2 molecules (see central cavity in Figure S18), although a single occupation per cavity gives lower energy. Molecules from the gas phase migrate through the crystal passing through transition state (TS) locations, labeled 'Y', when jumping between neighbour cavities (X ↔ Y ↔ X). Figure S19 shows the free microporous space of the MOF showing the larger size of 'X' cavities with respect to the TS region ('Y').

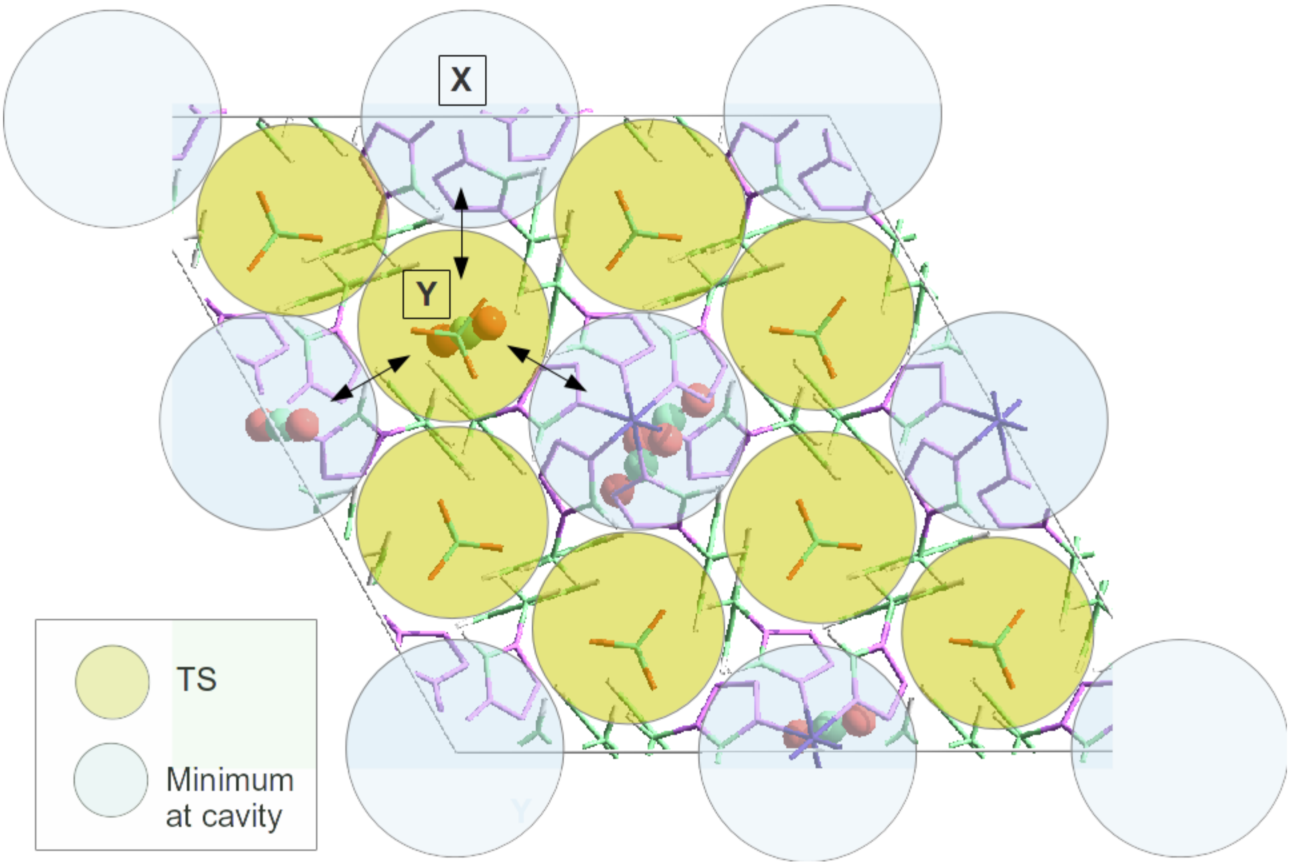

Figure S18. **CCP-1** view across [001] showing the different positions for molecular pathways. Cavities labelled 'X' (blue circles) are the minimum energy positions whilst the path connecting two 'X' is shown as green circles ('Y') and it corresponds to a higher energy (TS) in the diffusion path. Some CO_2 guest molecules are filling some cages just for illustration purposes.

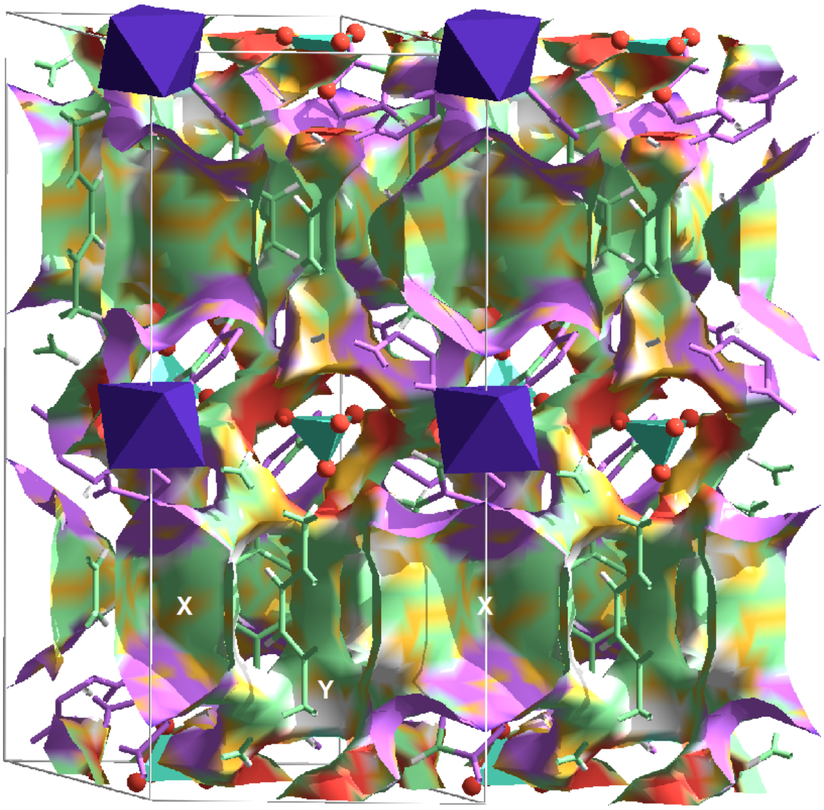

Figure S19. **CCP-1** view across [110] showing the microporous space. Cavities corresponding to the minimum energy of the CO_2 molecule are labelled as 'X'. The transition state region between two 'X' is labelled as 'Y'.

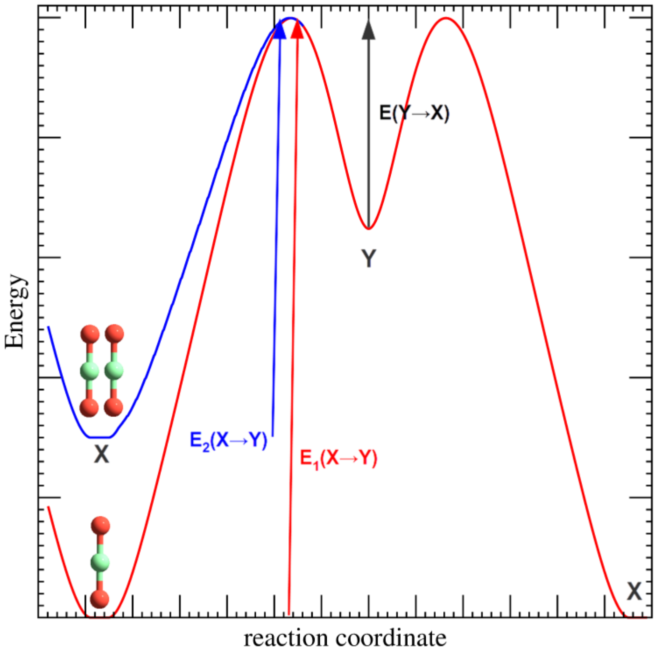

Figure S20. Energetic scheme corresponding to the diffusion of CO_2 through **CCP-1**. 'X' is the cavity corresponding to the minimum energy and 'Y' is a higher energy location. When two CO_2 molecules fill the 'X' cavity, their energy in the cavity increases, activating the diffusion.

The diffusion of CO_2 molecules has been simulated by molecular dynamics runs of 600 ps at different loading and temperatures. At 10 K the diffusion is so low that migration between cavities is not observed during the time of the simulation. It is expected that this migration will only be observed if the simulation time is increased at least two orders of magnitude, which goes beyond the scope of our current computational capabilities. Instead we have increased the temperature to 498 K in order to accelerate the dynamics and we have produced several runs. When only 1 CO_2 molecule fills the cavities ('X') we do not observe any jump between cavities. It is only when the population of the cavities increases to two CO_2 molecules that the jumps between cavities are observed. This is due to the fact the increasing $CO_2 \cdots CO_2$ repulsions lead to a higher energy of the CO_2 molecules inside the cavity 'X' (Figure S20). Then a decrease in the activation energy required for the migration is observed ($E_2 < E_1$, Figure S20) and the jumps between cavities are observed. The still low frequency of jumps does not allow to calculate with the sufficient accuracy the energy required for the intercavity migrations, and Figure S20 can only be regarded as a qualitative representation of the diffusion. Figure S21 shows the small space available for the jumps between cavities.

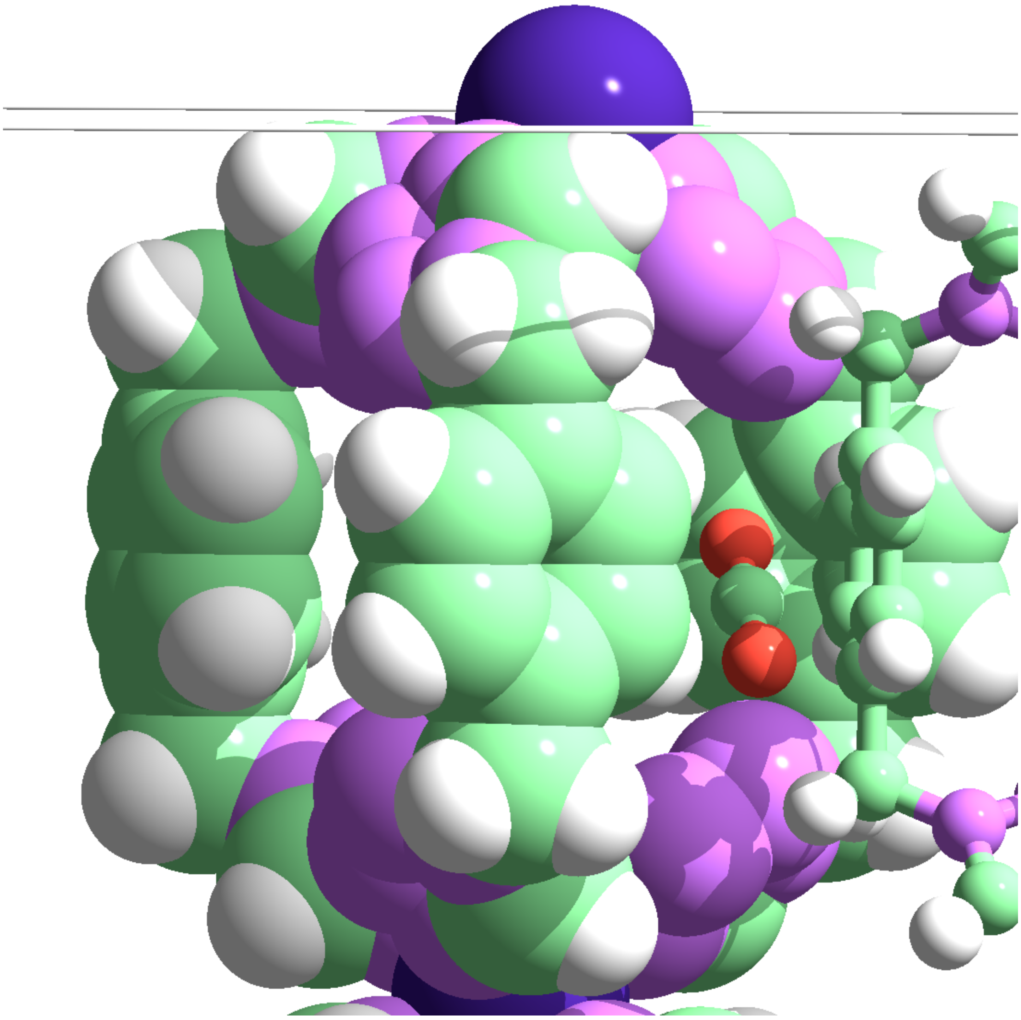

Figure S21. Fragment of the unit cell of **CCP-1** showing a cavity (larger balls) and a neighbour cavity (smaller balls) where two benzene rings define a narrow corridor through which a CO_2 molecule can jump from cage to cage.

A movie has been produced to show the mechanism of diffusion. The movie starts with 2 CO_2 molecules in a cavity ('X') and eventually a migration through a neighbour cavity ('X') is observed passing through the transition state region ('Y'), as indicated in Figure S22. In this migration, some phenyl rings are especially important as two of them define a gate for the first step ('X' → 'Y') and two of them define a gate for the second step ('Y' → 'X'). In Figure S22, a relevant distance between specific hydrogen atoms of phenyl rings has been defined. This distance measures the opening/closing of the gate that connects 'X' and 'Y'. A plot of this distance throughout the time of the simulation (Figure S23) shows the dynamics of the intercavity event. During the migration process the plotted H-H distance increases when the gate opens and then the migration is produced. The total duration of the jump can be estimated in ca. 135 ps. Our statistics are quite poor and with the current simulations we can only extract qualitative hints, but at least the mechanism of diffusivity has been unveiled.

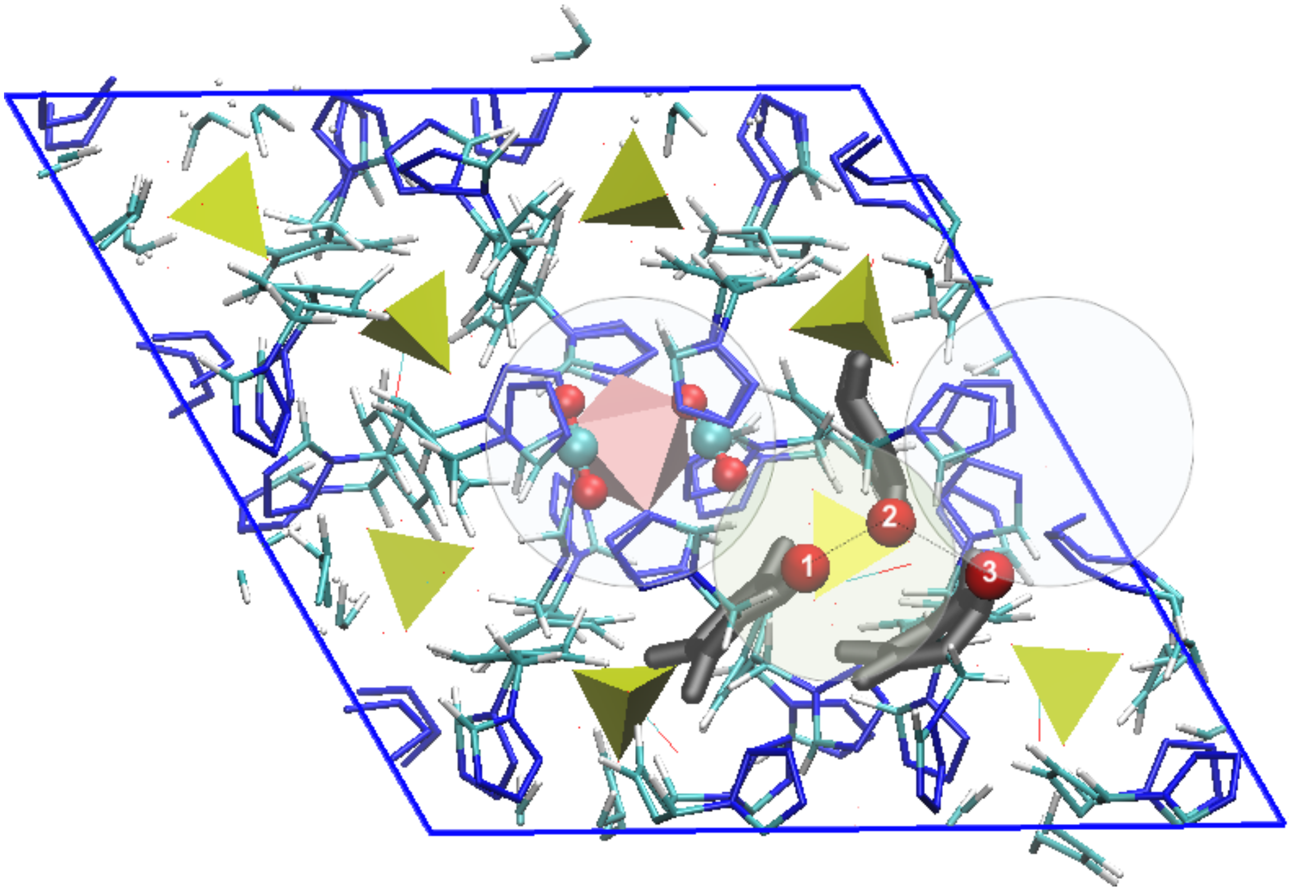

Figure S22. Scheme of the movie. A migration between two neighbour cavities ('X', larger circles) through a high-energy region ('Y', smaller circle) is observed (X → Y → X). In the first step (X → Y) a CO_2 molecule jumps through two neighbour phenyl rings where two relevant atoms are highlighted (1 and 2). In the second step (Y → X) the CO_2 molecule jumps through two another pair of neighbour phenyl rings where two relevant atoms are highlighted (2 and 3). The movie is available as Supporting Movie 1.

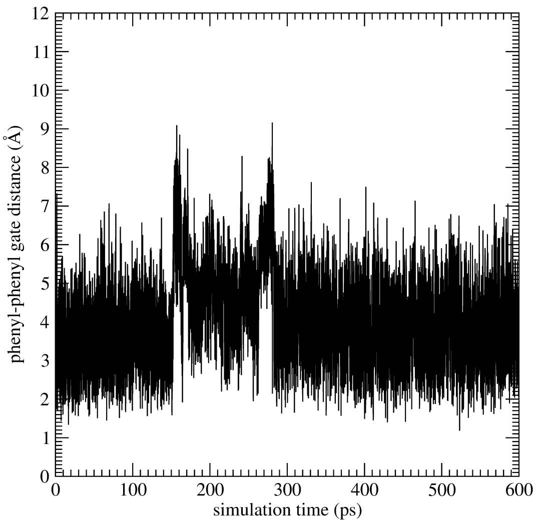

Figure S23. H-H gate opening in **CCP-1** during the 600 ps where an intercavity jump of a CO_2 molecule can be observed. The H atoms have been selected according to the scheme in Figure S22. The times at which the two steps (X → Y and Y → X) of the intercavity migration occurs are clearly observed ca 150 and 275 ps. The total duration of the migration can be estimated in ca. 135 ps.

Molecular dynamics methods

Molecular dynamics were performed using the widely used Universal force field (UFF)[S17] as well as a modified version (modified-UFF) that was employed in a previous work.[S18] Universal Force Field (UFF) has been used in previous studies with reasonable results for the two- three- and four-body interactions and here a modification has been introduced in the van der Waals interactions between CO_2 and the MOF. The dispersion interactions are expected to play an important role, and hence the modified-UFF contains the effect of dispersion interactions taken from quantum chemistry results. After some testing, the modified-UFF was shown to behave more correctly and was chosen for the molecular dynamics runs.

The GULP software (version 4.3.2)[S19] has been used, able to run in parallel for the evaluation of the energy and first derivatives using MPI, based on a replicated data algorithm. Molecular dynamics were carried out in the NVT ensemble using a timestep of 1 fs, and with relaxation times for thermostat and barostat set to 1 ps. Different temperatures, starting from 10 K, were sampled in order to try to observe the migration of the CO_2 molecules. The simulations showed here comprised two CO_2 molecules and run for 600 ps at 498 K.

A crucial parameter in our force field is the N-C-C-C dihedral term and we just point here its importance. This dihedral rotation (Figure S24) controls the possibility of benzene rings to rotate and make available space for diffusing CO_2 molecules. From the energy profile we do not appreciate a particularly high energetic penalty and we believe this is a correct parameter in our set up.

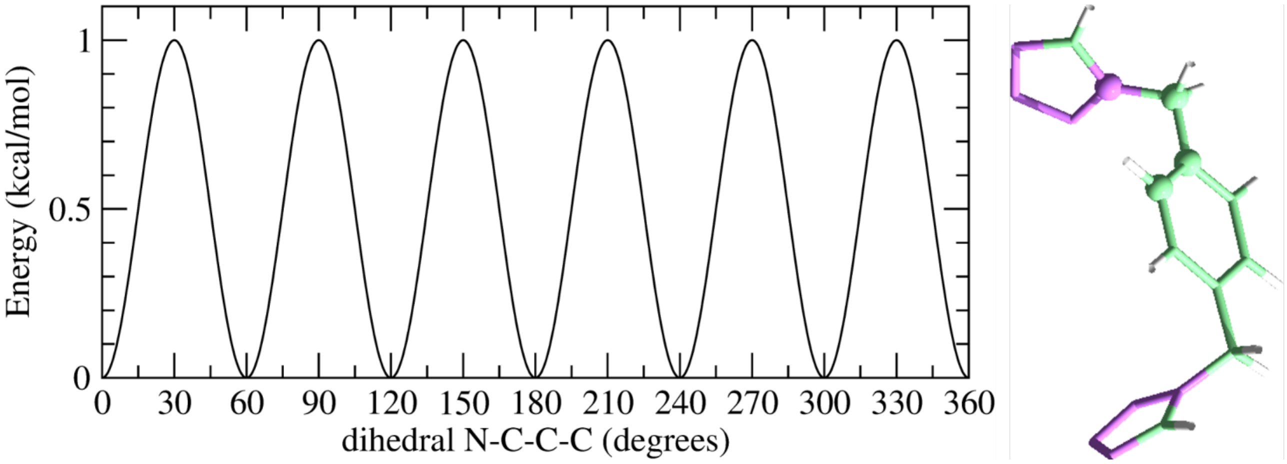

Figure S24. Energy (left) of rotation of the N-C-C-C dihedral angle (right) from the **CCP-1** structure. This dihedral is involved in benzene rotations for CO_2 diffusion (see Figure S21).

Coefficient diffusion

From Figure S25 it can be appreciated that the lack of linearity does not allow to fit the calculated data to a straight line and therefore it is not possible to give a value of the diffusion coefficient. For such a low process, much longer simulations (perhaps two orders of magnitude longer) would be needed. However, it is possible to advance from the data obtained that the diffusion coefficient will be below $20 \text{x} 10^{-8}$ $cm^2 \cdot s^{-1}$

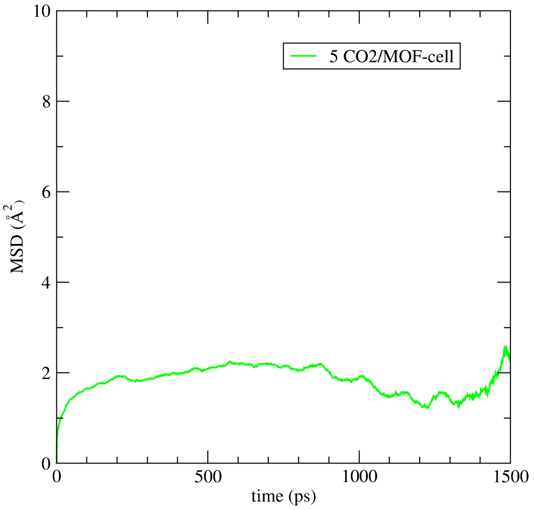

Figure S25. Mean-square displacement vs. simulation time obtained from the molecular dynamics simulation at 298 K. The loading corresponds to 5 CO_2 molecules per unit cell of MOF, with the chemical composition of the unit cell being $[Fe(bztx)_3]_8[ClO_4]_{16}$, the unit cell volume 9486.89 Å^3, and the cell parameters: a = 21.4290 Å, b = 21.3940 Å, c = 23.7319 Å, α = 90.0584 °, β = 90.1007 °, γ = 119.3122 °.

S13. Additional structural figures

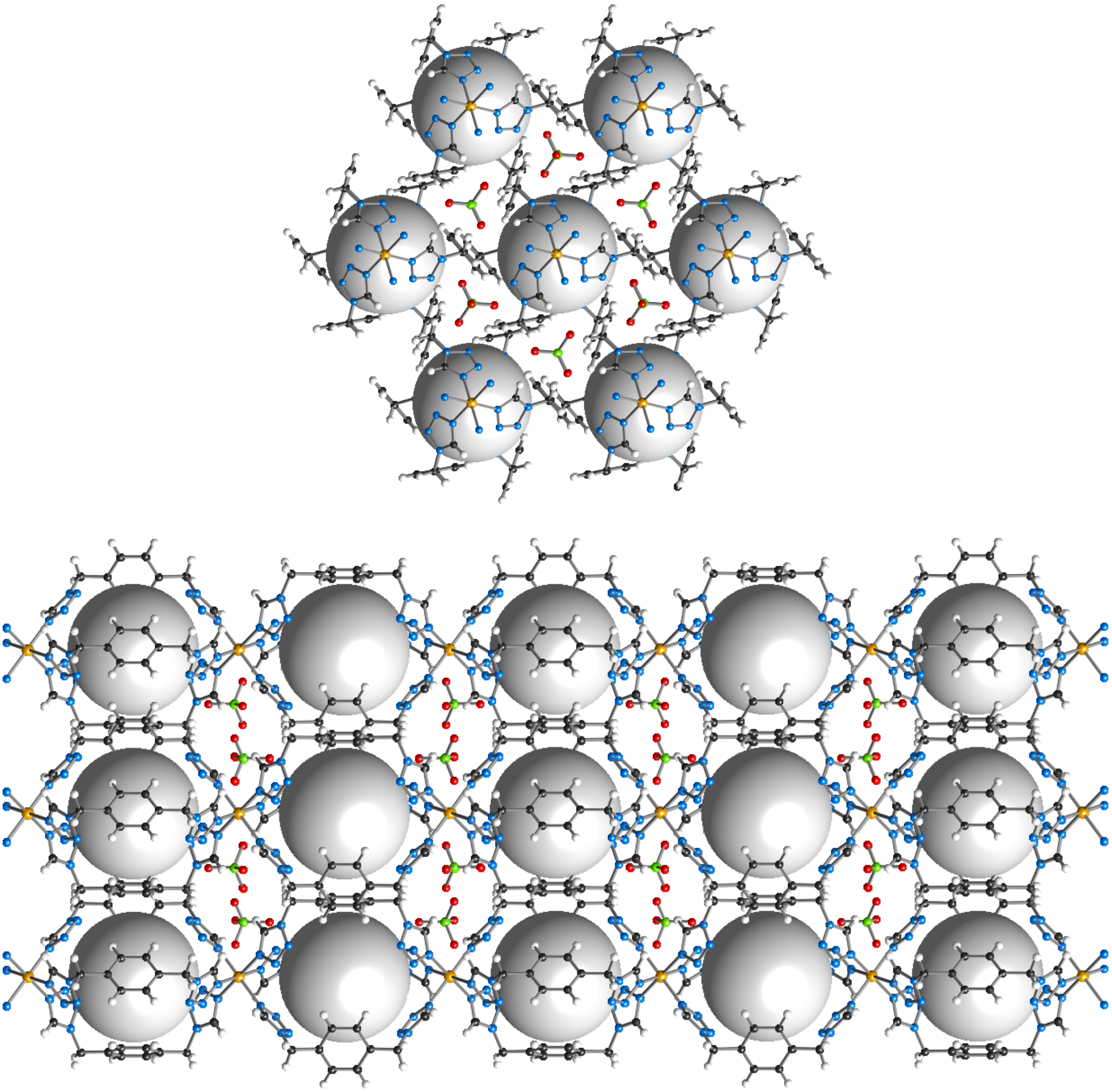

Figure S26. Two different views of the crystal packing of **CCP-1**, highlighting the discrete voids, which are not connected between each other.

S14. References

S1. Coronado, E.; Giménez-Marqués, M.; Mínguez Espallargas, G.; Rey, F.; Vitórica-Yrezábal, I. J. *J. Am. Chem. Soc.* **2013**, *135*, 15986–15989.

S2. Sheldrick, G. M. *Acta Crystallogr., Sect. A: Found. Crystallogr.* **2008**, *64*, 112.

S3. Pawley, G. S. *J. Appl. Cryst.* **1981**, *14*, 357.

S4. Coelho, A. A. TOPAS-Academic, Version 4.1, 2007, see: http:// www.topas-academic.net.

S5. Rietveld, H. M. *J. Appl. Crystallogr.* **1969**, *2*, 65.

S6. Li, J.-R.; Kuppler, R. J.; Zhou, H.-C., *Chem. Soc. Rev.* **2009**, *38*, 1477–1504.

S7. Coonan, M. H.; Ritchie, G. L. D. *Chem. Phys. Lett.* **1993**, *202*, 237–241.

S8. Crank, J., in *The Mathematics of Diffusion*, Oxford University Press, London, 1957.

S9 D. D. Do. Adsorption Analysis: Equilibria and Kinetics. Imperial College Press. London. 1998.

S10. Mitchell, P. C. H.; Parker, S. F.; Ramirez-Cuesta, A. J; Tomkinson, J. *Vibrational Spectroscopy with Neutrons, with Applications in Chemistry, Biology, Materials Science and Catalysis,* World Scientific, Singapore, 2005.

S11. Materials Studio 6.1 http://accelrys.com/products/datasheets/dmol3.pdf

S12. J. P. Perdew, K. Burke, M. Ernzerhof. Eratumn: Generalized Gradient Approximation Made Simple. Physical Review Letters, 78:1396, 1997.

S13. Ramirez-Cuesta, A. J. *Comp. Phys. Comm.* **157**, 226–238 (2004).

S14. Kresse, G., Furthmuller, J. 1996 Phys. Rev. B 54 11169

S15. Hinsen K., Pellegrini E., Stachura S. and Kneller G. R., 2012 J. Comput. Chem. 33 2043.

S16. Bée M., *Physica B* **1992**, *182*, 323–336.

S17. Rappe, S. A. K.; Casewit, C. J.; Colwell, K. S.; Goddard, W. A.; Skiff, W. M. *J. Am. Chem. Soc.* **1992**, *114*, 10593.

S18. Sastre, G.; van den Bergh, J.; Kapeijn, F.; Denysenko, D.; Volkmer, D. *Dalton Trans.* **2014**, *43*, 9612–9619.

S19. (a) Gale, J. D. *J. Chem. Soc. Faraday Trans.* **1997**, *93*, 629–637. (b) Gale, J. D.; Rohl, A. L. *Mol. Simul.* **2003**, *29*, 291–341.